

Marine boundary layer dust and pollutant transport associated with the passage of a frontal system over eastern Asia

Timothy S. Bates,^{1,2,3} Patricia K. Quinn,^{1,2} Derek J. Coffman,^{1,2} David S. Covert,^{2,3} Theresa L. Miller,^{1,2} James E. Johnson,^{1,2} Gregory R. Carmichael,⁴ Itsushi Uno,⁵ Sergio A. Guazzotti,⁶ David A. Sodeman,⁶ Kimberly A. Prather,⁶ Monica Rivera,⁷ Lynn M. Russell,⁸ and John T. Merrill⁹

Received 22 August 2003; revised 12 November 2003; accepted 25 November 2003; published 1 September 2004.

[1] Aerosol chemical composition and number size distributions were measured aboard the R/V *Ronald H. Brown* during the Asian Pacific Regional Aerosol Characterization Experiment (ACE-Asia) from 14 March to 20 April 2001. This manuscript focuses on the prefrontal and postfrontal air masses sampled aboard the ship in the Sea of Japan between 6 and 15 April 2001 to illustrate the different chemical sources/mixtures off the coast of Asia resulting from the contrasting meteorological transport patterns. The prefrontal air masses had a dominant accumulation mode composed of pollution and volcanic aerosols. The aerosol was predominately ammonium sulfate and organic carbon. Minor amounts of dust were present in the marine boundary layer (MBL) as a result of subsidence from a pronounced Taklimakan dust aerosol layer aloft. The sea salt in both the submicron and supermicron modes was highly depleted in chloride from reaction with sulfuric and nitric acid vapors. The passage of a large low-pressure center, surrounded by a widespread distribution of airborne dust, on 10 April brought elevated concentrations of submicron and supermicron Gobi desert dust to the ship. The supermicron dust particles contained high concentrations of sulfate, nitrate, organic, and elemental carbon. The MBL aerosol properties and controlling processes described here provide data to evaluate and refine chemical transport models. **INDEX TERMS:** 0305 Atmospheric Composition and Structure: Aerosols and particles (0345, 4801); 0322 Atmospheric Composition and Structure: Constituent sources and sinks; 0368 Atmospheric Composition and Structure: Troposphere—constituent transport and chemistry; **KEYWORDS:** aerosol chemistry, aerosol size distributions, ACE-Asia

Citation: Bates, T. S., et al. (2004), Marine boundary layer dust and pollutant transport associated with the passage of a frontal system over eastern Asia, *J. Geophys. Res.*, 109, D19S19, doi:10.1029/2003JD004094.

1. Introduction

[2] The chemical and physical properties of atmospheric aerosol particles control their radiative and cloud nucleating properties. Characterizing the regional distributions of aerosol properties and the processes controlling those distributions, therefore, is essential for assessing direct and indirect aerosol radiative forcing and developing a predictive understanding of the climatic impact of atmospheric aerosols. The atmospheric aerosol distributions off the east coast of Asia are particularly complex because of the large number of varied sources (mobilized mineral dust [*Xuan and Sokolik*, 2002], biomass and biofuel burning [*Bey et al.*, 2001; *Streets et al.*, 2001], volcanic, industrial and biogenic emissions [*Arndt et al.*, 1997; *Streets et al.*, 2001], ship emissions [*Streets et al.*, 2000] and sea-salt spray). These various aerosol components and their precursor gases interact as they are transported through the atmosphere to form a complex internal mixture generally dominated by two or more distinct modes. The resulting size distributions of different chemical components will thus affect their atmospheric lifetimes and radiative and cloud nucleating properties.

¹Pacific Marine Environmental Laboratory, NOAA, Seattle, Washington, USA.

²Joint Institute for the Study of the Atmosphere and Ocean, University of Washington, Seattle, Washington, USA.

³Department of Atmospheric Sciences, University of Washington, Seattle, Washington, USA.

⁴Center for Global and Regional Environmental Research, University of Iowa, Iowa City, Iowa, USA.

⁵Research Institute for Applied Mechanics, Kyushu University, Kasuga, Japan.

⁶Department of Chemistry and Biochemistry, University of California, San Diego, La Jolla, California, USA.

⁷Department of Environmental Engineering, Princeton University, Princeton, New Jersey, USA.

⁸Department of Chemical Engineering, Princeton University, Princeton, New Jersey, USA.

⁹Center for Atmospheric Chemistry Studies, Graduate School of Oceanography, University of Rhode Island, Narragansett, Rhode Island, USA.

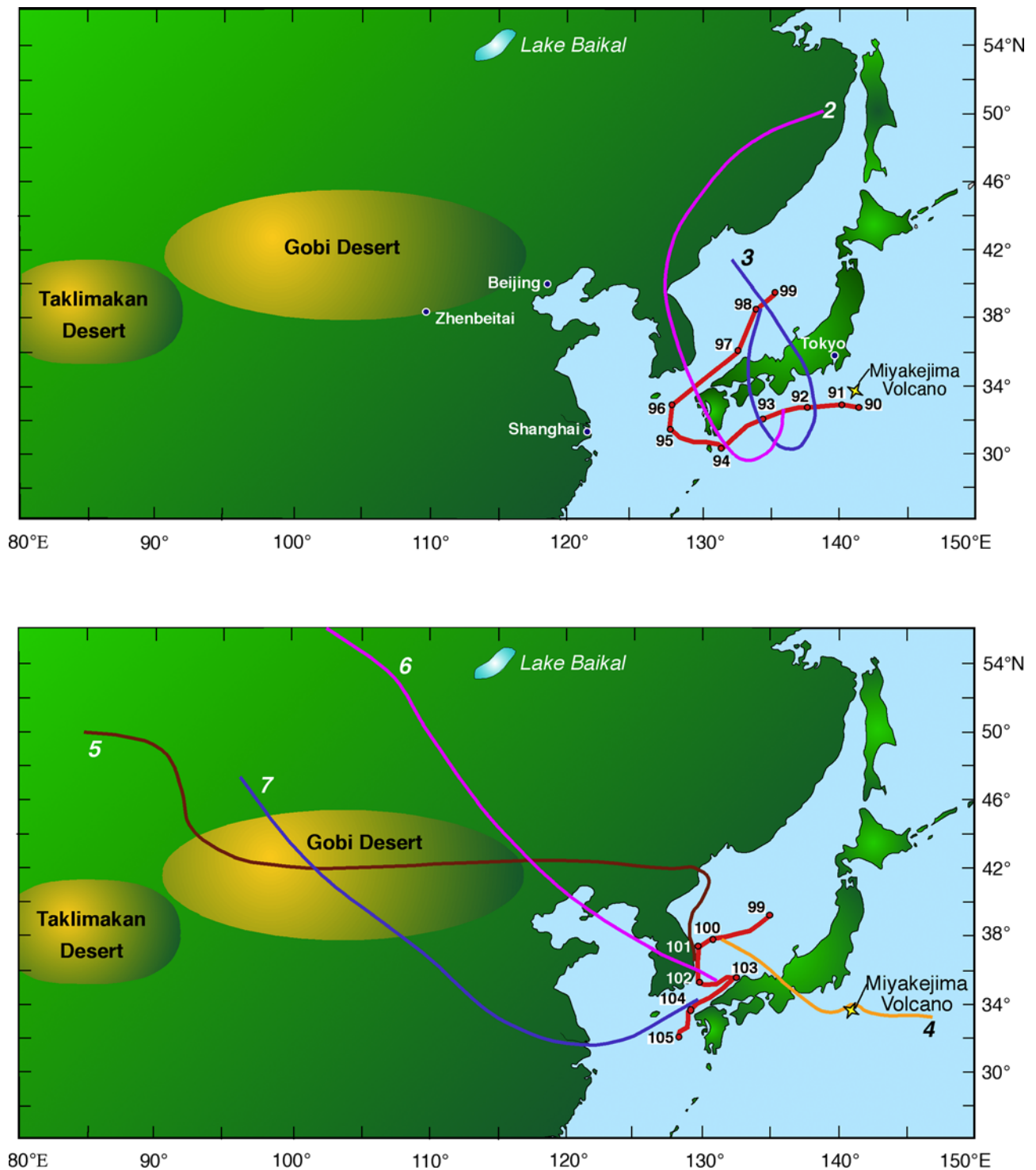


Figure 1. ACE-Asia NOAA R/V *Ronald H. Brown* cruise track from 31 March (DOY 90) to 15 April (DOY 105) 2001. The transit from Hawaii to Japan (DOY 73–90) and associated back trajectories are not shown here. The symbols indicate the beginning of each UTC day. Five day lower level (500 m) back trajectories are shown for DOY 92.25, 98.5, 100, 101.5, 102.5, and 103.75. The approximate locations of the Gobi and Taklimakan deserts are taken from *Sun et al.* [2001]. The Gobi desert refers to the vast hyperarid region of northern China and southern Mongolia north of Zhenbeitai and includes the Mu Us, Ulan Buh, Hobq, Tengger, and Badain Juran deserts [*Zhang et al.*, 2003a, 2003b].

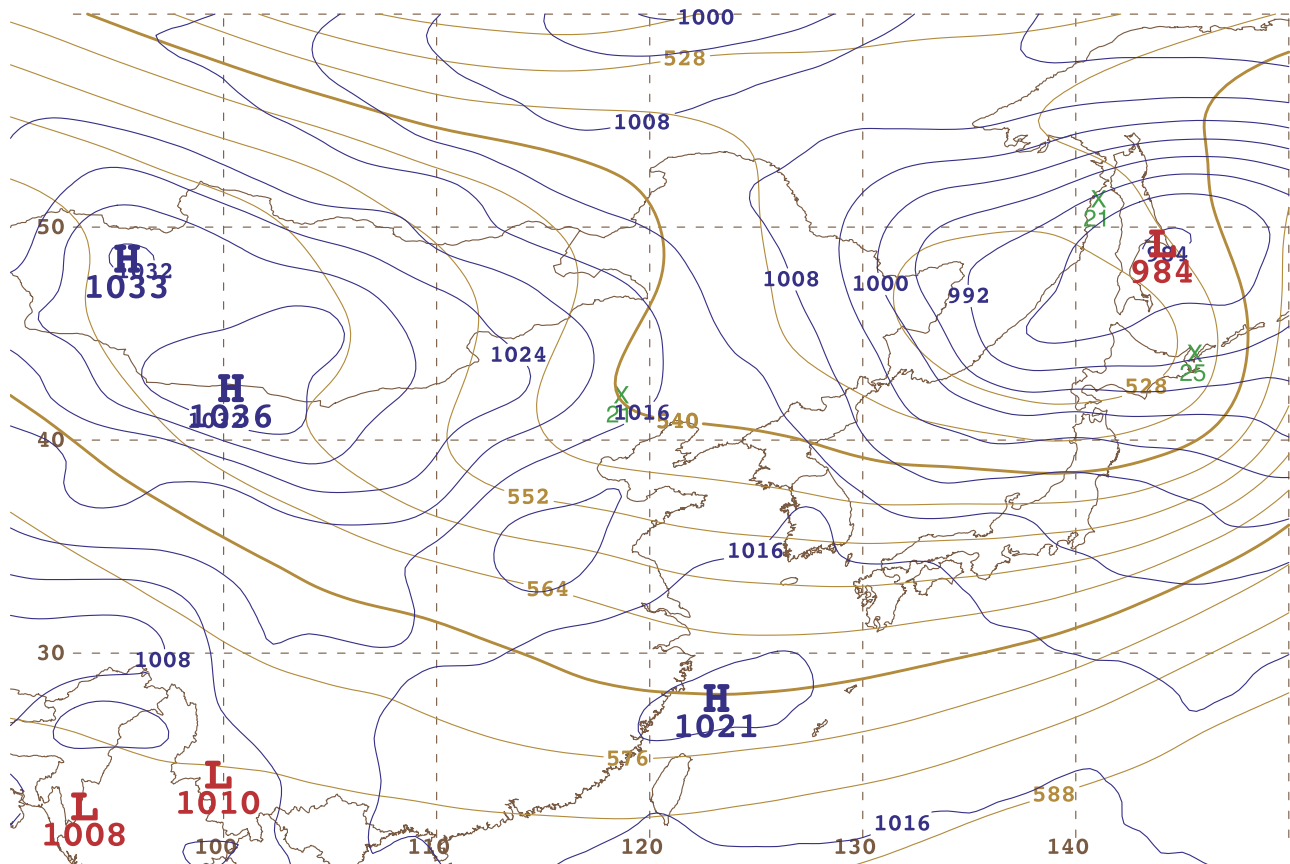


Figure 2. A composite meteorological chart from 0000 UTC on 13 April 2001 (DOY 103). The low center over northern Japan and the broad anticyclone south of Japan steered the postfrontal flow from northwest (DOY 102) to southwest (DOY 104). Mean sea level pressure contours (blue) at intervals of 4 hPa and 500 hPa geopotential height contours (tan, in dm) at intervals of 60 m are shown, along with 500 hPa vorticity extrema in conventional meteorological notation. The figure is based on the global analysis of the U.S. Navy NOGAPS model, plotted here at 1 degree resolution.

[3] Dust storms are of particular interest to both climate and air quality in east Asia and regions downwind. During the spring (March–May), Mongolian cyclonic depressions and the associated frontal system can generate intensive dust storms [Sun *et al.*, 2001]. The dust from the Taklimakan and Gobi deserts and pollution entrained downwind are transported out of Asia in distinct layers [Huebert *et al.*, 2003], with the highest pollution concentrations generally confined to the boundary layer, especially in postfrontal air mass [Anderson *et al.*, 2003; Chin *et al.*, 2003]. It is thus critical to understand the aerosol properties and controlling processes in this lowest layer of the atmosphere.

[4] During the International Global Atmospheric Chemistry (IGAC) Project's Asian Pacific Regional Aerosol Characterization Experiment (ACE-Asia) [Huebert *et al.*, 2003], we conducted shipboard measurements of marine boundary layer (MBL) aerosol properties and related parameters aboard the NOAA R/V *Ronald H. Brown* from 14 March to 20 April 2001. Here we report the chemical mass and physical number and volume distributions of the aerosols sampled in the MBL off the coast of Asia (Figure 1). In particular we highlight the prefrontal and postfrontal conditions between 6 and 15 April (day of year (DOY) 96–105) to illustrate the different chemical sources/

mixtures resulting from the contrasting meteorological transport patterns. The optical properties of these different chemical sources/mixtures are discussed in detail by Quinn *et al.* [2004], Carrico *et al.* [2003], and Conant *et al.* [2003].

2. Meteorological Summary

[5] A large low-pressure center, surrounded by a widespread distribution of airborne dust, crossed Mongolia/northern China between 8 and 11 April (DOY 98–101) and moved offshore north of 45°N. The frontal zone associated with this low-pressure center reached the ship at DOY 100.8 and slowed as it moved over the Sea of Japan. A low center formed east of the ship, along the frontal boundary in the Sea of Japan around DOY 101.5 and strengthened from its initial pressure of ~1000 hPa as it moved toward the NNE. The composite meteorological chart (Figure 2) shows the low center north of Japan, as well as a weak, broad anticyclone extending from 115°–140°E south of 35°N. The flow during this period, controlled by this low-pressure center north of Japan and broad anticyclone south of Japan, shifted from NW (DOY 102) to SW (DOY 104) (Figure 1).

[6] The data collected during the cruise were separated into seven source region categories on the basis of air mass back trajectories. The source regions are defined as the geographical region along which the air mass traveled for the 5 days prior to sampling at the ship. While the focus of this paper is the prefrontal and postfrontal periods from DOY 96 to 105 we include two earlier periods for comparison. The ship position is shown at the beginning of each day (DOY 90–105) in Figure 1.

2.1. Source Region 1: Marine (DOY 75–84)

[7] The ship transited from Hawaii to Japan during DOY 75–84. Low-level back trajectories (500 m) and Rn measurements on the ship showed that the air masses sampled at the ship had not been in contact with the continent during the five preceding days.

2.2. Source Region 2: Polluted, Korea/Japan (DOY 91–94)

[8] The ship transited along the southern coast of Japan during DOY 91–94. Back trajectories (500 m) show flow from Korea and/or Japan (1 to 2 days back) and northern China (3 to 5 days back). The weather was initially calm with higher winds (from 92.1 to end) and rain (DOY 92.5–92.8, 92.9–93.1) later in the period. The atmospheric boundary layer height (BLH) was 1 to 2 km at beginning and end of period and up to 8 km from 92.5 to 93.5.

2.3. Source Region 3: Polluted, Japan (DOY 96.5–99.2)

[9] The ship was sampling in the Sea of Japan during DOY 96.5–99.2. Low-level trajectories (100–500 m) show air circulating over Japan for several days. The boundary layer was very stable and low (initially 1 km, then <500 m), and the relative humidity (RH) high (75 to 95%).

2.4. Source Region 4: Volcano + Polluted (DOY 99.3–100.5)

[10] The ship was sampling in the Sea of Japan during DOY 99.3–100.5. The boundary layer was very stable and low (<500 m), and no precipitation was observed. Lower level trajectories (100–500 m) show flow over the Miyakejima volcano and Japan. Upper level trajectories were from the west across China and sometimes Korea. A distinct dust layer was observed at an altitude of 5 km that contributed to a high aerosol optical depth.

2.5. Source Region 5: Dust, Frontal Passage (DOY 101–101.3)

[11] The ship was sampling in the Western Sea of Japan during DOY 101–101.3. The frontal zone reached the ship at DOY 100.8 bringing a wind shift from south to north. Upper level trajectories were from the north China/Mongolia dust region while low-level trajectories extended across Korea and China. This was the first time that both lower (500 m) and upper (2500 m) level back trajectories indicated flow from the dust regions. Precipitation did not begin until DOY 101.3.

2.6. Source Region 6: Dust + Korea (DOY 101.8–103.4)

[12] The ship was sampling in the Southern Sea of Japan during DOY 101.8–103.4 in the cloud-free dust laden air

behind the front. Both the lower (500 m) and upper level trajectories crossed Korea and north China/Mongolia. The BLH varied between 1 and 3 km, and the RH was much lower (between 35 and 60%) than the previous periods.

2.7. Source Region 7: Dust + Shanghai (DOY 103.4–104.5)

[13] The ship was sampling in the Korean Strait during DOY 103.4–104.5. The lower (500 m) and upper (2500 m) level back trajectories crossed the north China/Mongolia dust region and passed through Shanghai. The BLH ranged from 1.5 to 3.5 km, and the RH ranged from 55 to 80%. Precipitation was observed at DOY 103.9.

3. Methods

3.1. Aerosol Sample Inlet

[14] Aerosol particles were sampled 18 m above the sea surface through a heated mast that extended 5 m above the aerosol measurement container. The mast was capped with a horizontal inlet nozzle that was rotated into the relative wind to maintain nominally isokinetic flow and minimize the loss of supermicron particles. Air entered the inlet through a 5-cm-diameter hole, passed through a 7 degree expansion cone, and then into the 20-cm-inner-diameter sampling mast. The flow through the mast was $1 \text{ m}^3 \text{ min}^{-1}$. Wind tunnel tests have shown that the transmission efficiency for particles with aerodynamic diameters less than $6.5 \mu\text{m}$ (the largest size tested) is greater than 95% [Bates *et al.*, 2002].

[15] The bottom 1.5 m of the mast were heated to establish a stable reference relative humidity (RH) for the sample air of $55 \pm 5\%$. A stable reference RH allows for constant instrumental size segregation in spite of variations in ambient RH and results in chemical, physical, and optical measurements which are directly comparable. In addition, measurement at a constant reference RH makes it possible, with the knowledge of appropriate growth factors, for end users of the data set (process, chemical transport, and radiative transfer models) to adjust the measured parameters to a desired relative humidity. A reference RH of 55% was chosen because it is above the crystallization humidity of most aerosol components and component mixtures [Carrico *et al.*, 2003]. For the atmospheric conditions encountered during ACE Asia, it was possible to maintain 55% RH without excessive heating of the aerosol. On average, the aerosol was heated 5.1°C above the ambient temperature. All results of the in situ measurements are reported at $55 \pm 5\%$ RH.

[16] Twenty-three 1.6 cm outer diameter stainless steel tubes extended into the heated portion of the mast. These were connected to the aerosol instrumentation and impactors with conductive silicon tubing to prevent electrostatic loss of particles. An exception to this was the lines connected to the impactors used for collection of carbonaceous aerosol, organic functional groups and the aerosol-time-of-flight mass spectrometer (ATOFMS); they were constructed of stainless steel.

[17] The airflow to the impactors was controlled so that air was sampled only when the concentration of particles greater than 15 nm in diameter indicated the sample air was free of local contamination (i.e., there were no rapid

increases in particle concentration), the relative wind speed was greater than 3 m s^{-1} , and the relative wind was forward of the beam.

3.2. Aerosol Chemical Composition

3.2.1. Impactor Sample Collection for Chemical Analysis

[18] Two-stage multijet cascade impactors [Berner *et al.*, 1979] sampling air at $55 \pm 5\%$ RH were used to determine submicron and supermicron concentrations of inorganic ions, organic and elemental carbon (OC and EC), and inorganic oxidized material (IOM). The 50% aerodynamic cutoff diameters of the impactors, $D_{50,\text{aero}}$, were 1.1 and $10 \mu\text{m}$. The RH of the sampled air stream was measured a few inches upstream from the impactors. Throughout the paper submicron refers to particles with $D_{\text{aero}} < 1.1 \mu\text{m}$ at 55% RH and supermicron refers to particles with $1.1 \mu\text{m} < D_{\text{aero}} < 10 \mu\text{m}$ at 55% RH.

[19] A $12 \mu\text{m}$ grease cup at the inlet of each impactor was coated with silicone grease to prevent the bounce of larger particles onto the downstream stages. A Tedlar film placed on the impactor jet plate having a $D_{50,\text{aero}}$ of $10 \mu\text{m}$ was sprayed with silicone lubricant for the same reason. Since films placed on downstream jet plates were used for chemical analysis, they were not sprayed to avoid contamination. All handling of the substrates was done in an NH_3 - and SO_2 -free glove box. Blank levels were determined by loading an impactor with substrates but not drawing any air through it. Sampling periods ranged from 2.5 to 7 hrs during the day and 4 to 12 hours at night.

3.2.2. Inorganic Ions

[20] Submicron and supermicron concentrations of Cl^- , NO_3^- , SO_4^{2-} , methanesulfonate (MSA^-), Na^+ , NH_4^+ , K^+ , Mg^{+2} , and Ca^{+2} were determined by ion chromatography (IC) [Quinn *et al.*, 1998]. Tedlar films were used as the collection substrate in the impaction stage and a Millipore Fluoropore filter ($1.0\text{-}\mu\text{m}$ pore size) was used for the backup filter. Prior to sampling, films were cleaned in an ultrasonic bath in 10% H_2O_2 for 30 min, rinsed in distilled, deionized water, and dried in the glove box. Postsampling, filters and films were wetted with 1 mL of spectral grade methanol. An additional 5 mL of distilled deionized water were added to the solution and the substrates were extracted by sonicating for 30 min.

[21] Non-sea-salt sulfate concentrations were calculated from Na^+ concentrations and the ratio of sulfate to sodium in seawater. Sea-salt aerosol concentrations were calculated as

$$\text{sea salt} (\mu\text{g m}^{-3}) = \text{Cl}^- (\mu\text{g m}^{-3}) + \text{Na}^+ (\mu\text{g m}^{-3}) \times 1.47, \quad (1)$$

where 1.47 is the seawater ratio of $(\text{Na}^+ + \text{K}^+ + \text{Mg}^{+2} + \text{Ca}^{+2} + \text{SO}_4^{2-} + \text{HCO}_3^-)/\text{Na}^+$ [Holland, 1978]. This approach prevents the inclusion of non-sea-salt K^+ , Mg^{+2} , Ca^{+2} , SO_4^{2-} , and HCO_3^- in the sea-salt mass and allows for the loss of Cl^- mass through Cl^- depletion processes. It also assumes that all measured Na^+ and Cl^- is derived from seawater. Results of Savoie and Prospero [1980] indicate that soil dust has a minimal contribution to measured soluble sodium concentrations.

[22] Sources of uncertainty in the ionic mass include the air volume sampled (5%), the extract liquid volume (3.3%),

2 times the standard deviation of the blank values measured over the course of the experiment, and the precision of the method (2 times the standard deviation of repeated injections of a single sample).

3.2.3. Organic and Elemental Carbon

[23] Submicron and sub- $10 \mu\text{m}$ samples were collected using 2 and 1 stage impactors, respectively. Aluminum foils were used as substrates on the $1.1 \mu\text{m}$ jet plate. Each impactor had 2 quartz backup filters. All substrates were prebaked at 500°C prior to sampling. The sub- $10 \mu\text{m}$ and one submicron impactor were run without a denuder upstream. A second submicron impactor was run with a denuder upstream. The denuder was 30 cm long, contained 18 parallel strips of carbon-impregnated glass (CIG) fiber filters separated by 1.8 mm, and had a cross-sectional area of 9.6 cm^2 .

[24] The submicron OC data are from the denuder/impactor sampler. The last backup quartz filter in line was used as the blank. Submicron EC data are the average of the two submicron impactor samples (with and without denuders). The supermicron OC data are the difference between the sub- $10 \mu\text{m}$ and submicron impactors run without denuders. Impactors without denuders upstream were used for the supermicron OC determination in order to avoid losses of large particles in the denuder. OC concentrations from both impactors were corrected for blanks and artifacts using the last quartz filter in line. Supermicron EC data are the difference between the sub- $10 \mu\text{m}$ and the average of the two submicron impactor samples (with and without denuders).

[25] OC and EC concentrations were determined with a Sunset Labs thermal/optical analyzer [Birch and Cary, 1996]. The thermal program was the same as that used by other groups in ACE Asia [Schauer *et al.*, 2003]. Four temperature steps were used to achieve a final temperature of 870°C in He to drive off OC. After cooling the sample down to 550°C , a He/ O_2 mixture was introduced and the sample was heated in four temperature steps to 910°C to drive off EC. The transmission of light through the filter was measured to separate EC from any OC that charred during the initial stages of heating.

[26] No correction was made for carbonate carbon so OC includes both organic and carbonate carbon. The carbonate carbon was never more than 10% of the total OC, however. On the basis of an interlaboratory comparison of punches from four high-volume samples and two blanks, the agreement between 8 Sunset Labs carbon analyzers was within 4% for moderate level OC, within 13% for low-level OC, and within 13% for EC [Mader *et al.*, 2003; Schauer *et al.*, 2003].

[27] The mass of particulate organic matter (POM) was determined by multiplying the measured organic carbon concentration in $\mu\text{g m}^{-3}$ by a factor of 2.1 in the marine region and 1.6 elsewhere. The POM factor is an estimated average of the molecular weight per carbon weight and is based on a review of published measurements of the composition of organic aerosol in urban and nonurban regions [Turpin and Lim, 2001]. On the basis of the range of values given by Turpin and Lim [2001], the POM factor has an uncertainty of $\pm 31\%$.

[28] The uncertainties associated with positive and negative artifacts in the sampling of semivolatile organic species

can be substantial [Turpin *et al.*, 1994, 2000]. An effort was made to minimize and assess positive (adsorption of gas-phase species) and negative (volatilization of aerosol organic species which may have resulted from the pressure drop across the impactor and filter) artifacts by using a denuder upstream of the impactor and by comparing undenuded and denuder-filter samplers. Results from these comparisons have shown that after correcting for sampling artifacts, measured OC concentrations can vary by 10% between samplers [Mader *et al.*, 2003]. Other sources of uncertainty in the POM mass include the air volume sampled (5%), the area of the filter (5%), 2 times the standard deviation of the blanks measured over the course of the experiment ($0.44 \mu\text{g}/\text{cm}^2$), the precision of the method (5%) based on the results of Schauer *et al.* [2003], and the POM factor (31%).

[29] Sources of uncertainty in the EC mass include the air volume sampled (5%), the area of the filter (5%), 2 times the standard deviation of the blank values measured over the course of the experiment ($0.22 \mu\text{g cm}^{-2}$), and the precision of the method (5%) based on the results of Schauer *et al.* [2003].

3.2.4. Inorganic Oxidized Material (Dust)

[30] Total elemental composition (Na, Mg, Al, Si, P, Cl, K, Ca, Ti, V, Cr, Mn, Fe, Ni, Cu, Zn, Ba, As, and Pb) was determined by thin-film X-ray primary and secondary emission spectrometry [Feely *et al.*, 1991, 1998]. Submicron and sub-10 μm samples were collected on 1.0 μm pore size Teflo filters using 2 and 1 stage impactors, respectively. Supermicron elemental concentrations were determined by difference between the submicron and sub-10 μm samples. This method of sample collection allows for the sharp size cut of the impactor while collecting a thin film of aerosol necessary for the X-ray analysis. Filters were weighed before and after sample collection as described below.

[31] A component composed of inorganic oxidized material (IOM) was constructed from the elemental data. The IOM most likely was composed of soil dust and/or fly ash. These two components are difficult to distinguish on the basis of elemental ratios. To construct the IOM component, the mass concentrations of Al, Si, Ca, Fe, and Ti, the major elements in soil and fly ash, were combined. It was assumed that each element was present in the aerosol in its most common oxide form (Al_2O_3 , SiO_2 , CaO , K_2O , FeO , Fe_2O_3 , TiO_2) [Seinfeld, 1986]. The measured elemental mass concentration was multiplied by the appropriate molar correction factor as follows [Malm *et al.*, 1994; Perry *et al.*, 1997]:

$$[\text{IOM}] = 2.2[\text{Al}] + 2.49[\text{Si}] + 1.63[\text{Ca}] + 2.42[\text{Fe}] + 1.94[\text{Ti}]. \quad (2)$$

This equation includes a 16% correction factor to account for the presence of oxides of other elements such as K, Na, Mn, Mg, and V that are not included in the linear combination. In addition, the equation omits K from biomass burning by using Fe as a surrogate for soil K and an average K/Fe ratio of 0.6 in soil [Braaten and Cahill, 1986]. Noncrustal K was calculated using the K/Al ratio (0.31) of Asian loess [Jahn *et al.*, 2001].

[32] Sources of uncertainty in the IOM mass concentration include the volume of air sampled (5%), the area of the

filter (5%), the molar correction factor (6%), 2 times the standard deviation of the blank values measured over the course of the experiment for each element, and the precision of the X-ray analysis [Feely *et al.*, 1991].

3.2.5. Individual Particle Analysis (ATOFMS)

[33] The size and chemical composition of individual aerosol particles were measured with an aerosol-time-of-flight mass spectrometer (ATOFMS). The ATOFMS couples aerodynamic particle sizing with time-of-flight mass spectrometry in a single instrument, providing both positive and negative ion mass spectra for each detected particle [Prather *et al.*, 1994; Noble and Prather, 1996; Gard *et al.*, 1997]. Particles were classified into 17 exclusive classes (e.g., sea salt with sulfate, dust with sulfate) by carrying out searches for ions of interest with specific threshold values [e.g., Gard *et al.*, 1998; Silva *et al.*, 1999; Liu *et al.*, 2000; Angelino *et al.*, 2001; Guazzotti *et al.*, 2001]. The presence of nitrate in sea salt and dust particles was evaluated by the occurrence of signals at mass-to-charge (m/z) ratios $-46 [\text{NO}_2]^-$, $-62 [\text{NO}_3]^-$, $+30 [\text{NO}]^+$, or $+108 [\text{Na}_2\text{NO}_3]^+$ with the generic spectral characteristics of sea salt or dust. Similarly, sulfate was identified by peaks at m/z $-97 [\text{HSO}_4]^-$, $-80 [\text{SO}_3]^-$, $-96 [\text{SO}_4]^-$, or $+165 [\text{Na}_3\text{SO}_4]^+$ [Guazzotti *et al.*, 2001]. Further details about the ACE-Asia ATOFMS measurements are given by S. A. Guazzotti *et al.* (Regional and temporal variability in the chemical composition of individual particles during ACE-Asia, submitted to *Journal of Geophysical Research*, 2003).

3.2.6. Organic Functional Groups

[34] Forty L min^{-1} of the 55% RH sample stream from the sampling mast were pulled through an impactor ($D_{50,\text{aero}} = 1.0 \mu\text{m}$) and two virtual impactors [Sioutas *et al.*, 1994] in series to increase the concentration of the sample aerosol by up to a factor of 5 prior to collection on 37 mm stretched Teflon filters (Teflo 1 μm pore size, Pall Corporation, Ann Arbor, Michigan). A size-dependent concentration factor was determined in the laboratory by using NaCl aerosol for a broad size range by comparing particle number size distributions upstream and downstream of the concentrator using a differential mobility analyzer (TSI model 3071) and an aerodynamic particle sizer (TSI model 3320). A mass average concentration factor was determined for each sample using the laboratory measured size-dependent concentration factors and ambient size distributions measured aboard the ship. The mass averaged concentrations factors during the project ranged from 3 to 4.

[35] All sample handling was done with powder-free vinyl gloves and Teflon-coated tweezers. After collection, samples were placed in polystyrene petri dishes (Pall Corporation), sealed with Teflon tape and stored frozen until analysis. The filter samples were analyzed using a Mattson Research Series 100 FTIR spectrometer with a deuterated triglycine sulfate (DTGS) detector and a He-Ne laser. FTIR spectra were collected in transmission mode for each filter by averaging 200 absorbance scans at wave numbers from 400 to 4000 cm^{-1} with a resolution of 4 cm^{-1} . Teflon filters were scanned prior to use, and the resulting spectra were subtracted from scans after sampling to obtain the absorbance of the sampled aerosol. Filter support rings were etched to ensure that alignment was maintained during consecutive scans. Further details on the sampling protocol are given by Maria *et al.* [2002].

[36] The combined uncertainty for FTIR detection, peak integration, and adsorption artifacts are between 5% and 22% [Russell, 2003]. Uncertainties associated with the impactor sampling are not included here since only relative concentrations of the functional groups are reported.

3.3. Sulfur Dioxide

[37] Air was pulled from 18 m above sea level down the 20-cm-ID powder-coated aluminum aerosol sampling mast (6 m) at approximately $1 \text{ m}^3 \text{ min}^{-1}$. At the base of the sampling mast a 0.5 L min^{-1} flow was pulled through a 0.32-cm-inner-diameter, 1-m-long Teflon tube, a Millipore Fluoropore filter (1.0- μm pore size) housed in a Teflon filter holder, a Perma Pure, Inc., Nafion Drier (MD-070, stainless steel, 61 cm long) and then through 2 m of Teflon tubing to a Thermo Environmental Instruments model 43C trace level pulsed fluorescence analyzer. The initial 1 m of tubing, filter and drier were located in the humidity controlled (55%) chamber at the base of the mast. Dry zero air (scrubbed with a charcoal trap) was run through the outside of the Nafion Drier at 1 L min^{-1} . The analyzer was run with two channels (0–20 ppb full scale and 0–100 ppb full scale) and a 20 s averaging time. Data were recorded every minute.

[38] Zero air was introduced into the sample line upstream of the Fluoropore filter for 10 min every hour to establish a zero baseline. An SO_2 standard was generated with a permeation tube held at 50°C . The flow over the permeation tube, diluted to 17.7 ppb, was introduced into the sample line upstream of the Fluoropore filter for 10 min every 6 hours. The limit of detection for the 1 min data, defined as 2 times the standard deviation of the signal during the zero periods, was 170 ppt. For 30 min data the limit of detection was reduced to 30 ppt. Uncertainties in the concentrations based on the permeation tube weight and dilution flows is $<5\%$.

3.4. Number Size Distributions

[39] One of the 23 mast tubes was used to supply ambient air to an ultrafine differential mobility particle sizer (UDMPS), a differential mobility particle sizer (DMPS) and an aerodynamic particle sizer (APS, TSI model 3320). The two DMPSs were located in a humidity-controlled box (RH = $55 \pm 5\%$) at the base of the mast. The UDMPS was a short-column instrument [Winklmayr et al., 1991] connected to a TSI 3025 particle counter (TSI, St. Paul, Minnesota) operating with a positive center rod voltage to sample particles with a negative charge. Data were collected in 17 size bins from 3 to 26 nm geometric diameter. The UDMPS operated with an aerosol flow rate of 1 L/min and a sheath airflow rate of 10 L/min. The DMPS was a medium length column instrument connected to a TSI 3760 particle counter operating with a positive center rod voltage to sample particles with a negative charge. Data were collected in 17 size bins from 20 to 671 nm diameter. The DMPS operated with an aerosol flow rate of 0.5 L/min and a sheath airflow rate of 5 L/min. The relative humidity of the sheath air for both DMPSs was controlled resulting in a measurement RH in the DMPSs of approximately 55%. With this RH control the aerosol should not have effloresced if it was hydrated in the atmosphere [Carrico et al., 2003]. Mobility distributions were collected every 15 min.

[40] The mobility distributions from the UDMPS and DMPS were inverted to a number distribution assuming a Fuchs-Boltzman charge distribution from the K_1^{85} charge neutralizer [Stratman and Wiedensohler, 1997]. The overlapping channels between the two instruments were eliminated in the inversion. The data were corrected for diffusional losses [Covert et al., 1997] and size-dependent counting efficiencies based on pre-ACE-2 intercalibration exercises [Wiedensohler et al., 1997]. During ACE-Asia, the ratio of the total particle number measured by an independent TSI 3760 particle counter ($D_p > 13 \text{ nm}$) to the integrated number concentration from the UDMPS and DMPS of particles with $D_p > 13 \text{ nm}$ averaged $1.15 \pm 0.21\%$ (one standard deviation). The estimated uncertainty in the number concentration in each bin, based on flow uncertainties, is $\pm 10\%$.

[41] The APS was located in the lower humidity controlled box at the base of the mast. Although the APS inlet humidity was maintained at $55 \pm 5\%$ RH, internal heating of the sample in the APS by its sheath flow and waste heat may have reduced the measurement RH below 55% RH. The sheath flow was conditioned outside the instrument case before reintroduction into the sheath and acceleration nozzle but the temperature at the APS sensing volume was not measured. The instrumental temperature sensors near the sensing volume of the APS showed a temperature difference of about $+2^\circ\text{C}$ compared to the inlet temperature, but the sensing volume temperature may have been more or less than this. The effect of an RH change on the large aerosol particles at this point is difficult to quantify because the time for equilibration in the inlet jets is short. The RH is assumed to be above the efflorescence point of sea salt.

[42] Number size distributions were collected with the APS every 15 min averaged over the 13 min of the DMPS scan. The APS data were collected in 51 size bins with the nominal manufacturers aerodynamic diameters ranging from 0.542 to 20 μm . Data were corrected for phantom counts assuming that the counts in the largest 4 channels ($D_{\text{aero}} = 16$ to 20 μm) were phantom counts and that value was subtracted from the entire APS distribution. This correction resulted in a Junge slope of the number distribution that was nearly constant for $D_p > 5 \mu\text{m}$ and a volume concentration that varied randomly about zero for $D_p > 10 \mu\text{m}$. The APS data were corrected for ultra-Stokesian conditions in the instrument jet and nonspherical shape [Wang and John, 1987; Cheng et al., 1990, 1993; Wang et al., 2002]. On the basis of the coarse-mode chemical concentration, the aerosol measured in source regions 1, 2, and 4 were assigned a spherical shape, source regions 3 and 5 were assigned a doublet-sphere shape factor and source regions 6 and 7 were assigned a triplet-sphere shape factor [Quinn et al., 2004]. Finally, the APS data were converted from aerodynamic diameters to geometric diameters using calculated densities and the water masses associated with the inorganic ions at 55% RH. The densities and associated water masses were calculated with a thermodynamic equilibrium model (AeRho) using the measured chemical data [Quinn and Coffman, 1998]. The estimated uncertainty in the supermicron size distribution include particle sizing ($\pm 3\%$), the instrumental counting efficiency ($\pm 5\%$), and the shape factor ($\pm 17\%$ for a doublet and $\pm 22\%$ for a triplet). The error in the shape factor was based on the

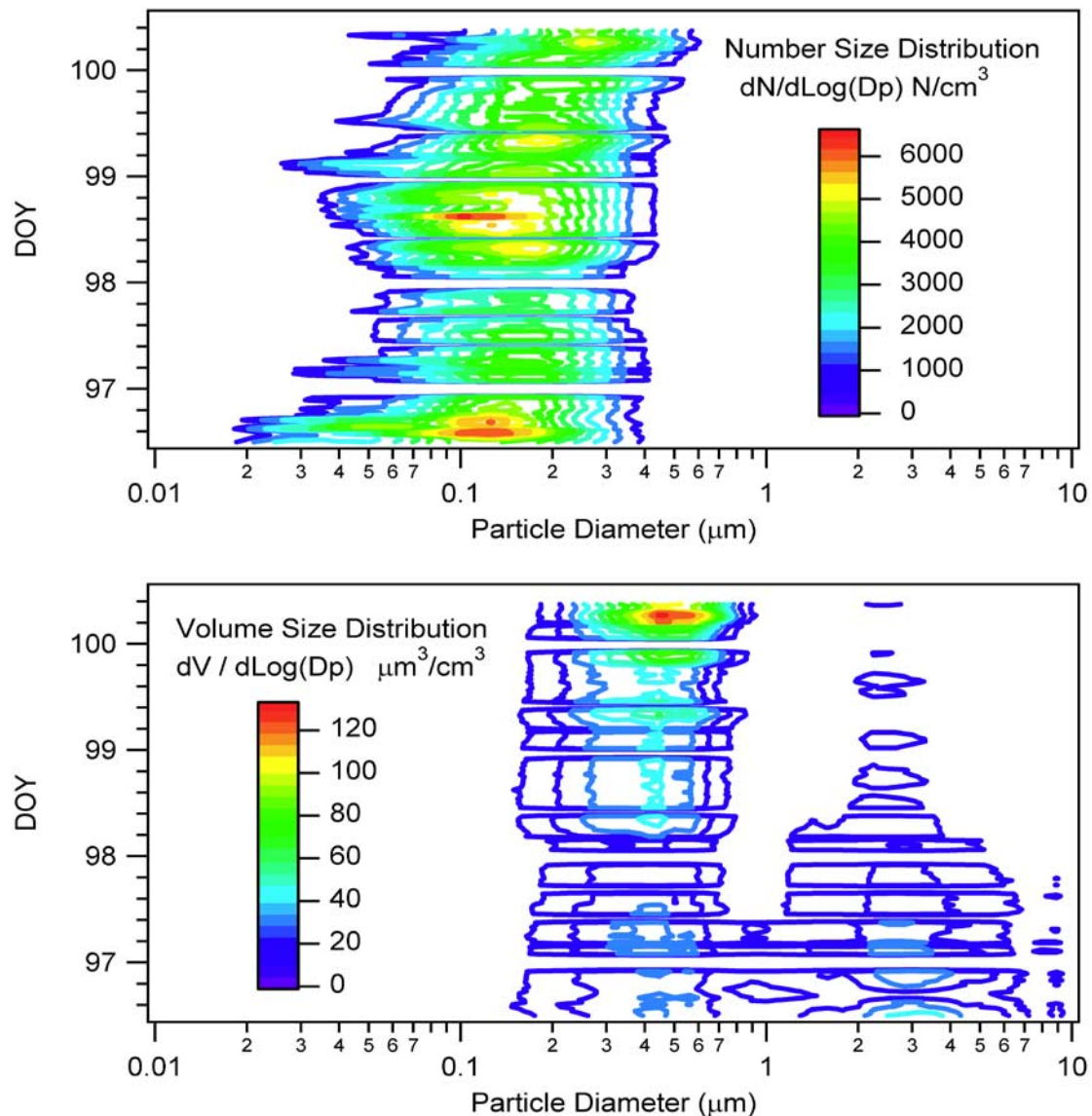


Figure 3. Particle number and volume size distributions (geometric diameter) in the prefrontal air mass (source regions 3 and 4) over the Sea of Japan between DOY 96.5 and 100.5.

percent change in size resulting from its use and, hence, most likely is an upper bound.

3.5. Additional Measurements

[43] Also measured were meteorological parameters including surface temperature, RH, wind speed and direction, as well as vertical profiles of these parameters from radiosondes. Air mass back trajectories were calculated at three arrival altitudes (500, 2500, and 5500 m) for the ship's position at 6 hour intervals. In cases where a temperature inversion occurred at a sub-500 m height (Polluted – Japan and Volcano + Polluted), additional trajectories were calculated for 50 and 100 m arrival heights. Trajectories were calculated with the hybrid-coordinate model HY-SPLIT 4 (Draxler [1992] and <http://www.arl.noaa.gov/ready/hysplit4.html>) using wind fields from the U.S. National Centers for Environmental Prediction Global Forecast System; these fields were at 191 km horizontal resolution

and were available at 6 hour intervals. All references to time are reported here in UTC. Dates are given as day of year (DOY), where noon on 1 February equals DOY 32.5.

4. Results and Discussion

4.1. Number and Volume Size Distributions

[44] The particle number size distributions in the shallow MBL prefrontal air mass (DOY 96.5 to DOY 100.5) were highly variable with several modes in each distribution in the size range between 0.04 and 0.4 μm geometric diameter. The aerosol measured at the ship was 1–2 days downwind of Japan and appeared to have undergone minimal cloud processing on the basis of the multimodal distribution and lack of any clear minima between the modes [Hoppel *et al.*, 1986; Bates *et al.*, 2002]. The center of the dominant mode during this period increased from 0.13 to 0.25 μm (Figure 3) with the most dramatic increase in modal diameter occur-

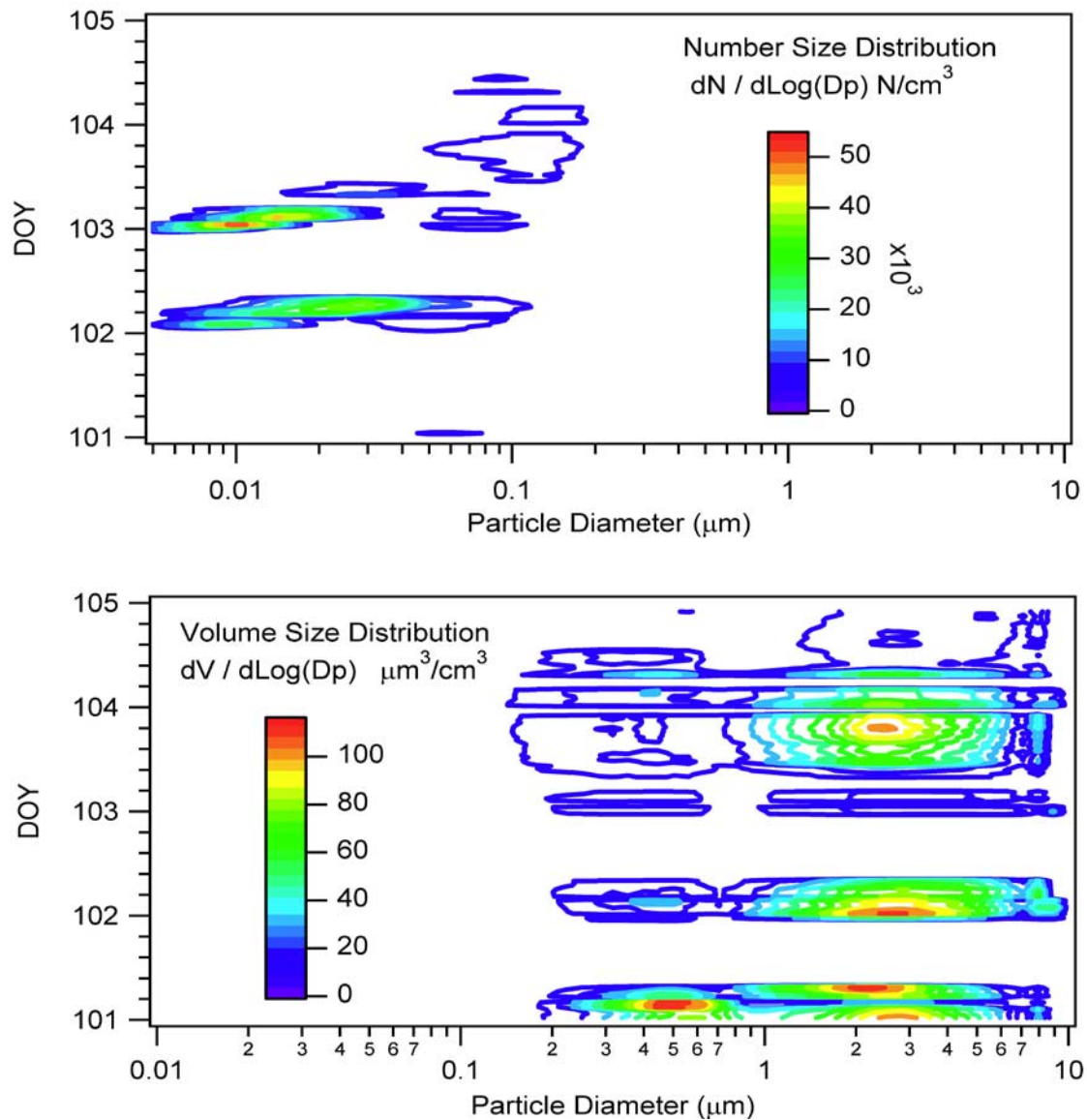


Figure 4. Particle number and volume size distributions (geometric diameter) in the postfrontal air mass (source regions 5, 6 and 7) over the Sea of Japan between DOY 101 and 105.

ring during the latter part of this time period (DOY 100–100.5) in the air mass influenced by the Miyakejima volcano.

[45] The particle volume size distribution in the prefrontal MBL air mass (DOY 96.5 to DOY 100.5) was initially bimodal with an accumulation and coarse mode (Figure 3). In the latter part of this time period the coarse mode decreased while the accumulation mode increased leaving a dominant accumulation mode volume distribution. This change was due to a decreasing wind speed which reduced the amount of sea-salt aerosol and an increasingly strong inversion capping the boundary layer which decreased the subsidence of dust from aloft and “concentrated” the pollution aerosol in the lower MBL.

[46] The passing frontal zone on DOY 100.8 ventilated the MBL bringing dust laden air down to the surface. The volume size distribution showed an initial peak of coarse-

mode aerosol, followed by a peak of “prefrontal” accumulation-mode aerosol, and finally a return to the “dust-dominated” coarse-mode aerosol (see section 4.2) in the period from DOY 101.0–101.3 (Figure 4). Either an irregularity along the front or vertical mixing could have brought the warm prefrontal air back to the ship as the slope of the frontal zone was upward into the cool/dry air. The ship measured two additional peaks of dust-dominated aerosol centered on DOY 102.0 (source region 6) and DOY 103.7 (source region 7) (Figure 4). On DOY 102 a broad high to the west resulted in NW winds that crossed the arid regions of China, the Yellow Sea, and Korea before arriving at the ship. Although the winds measured at the ship on DOY 103.7 were from the SW, calculated back trajectories show that the air mass passed over the arid regions of China, went offshore near Shanghai and changed direction when it encountered a transient anticyclone near 124 degrees E.

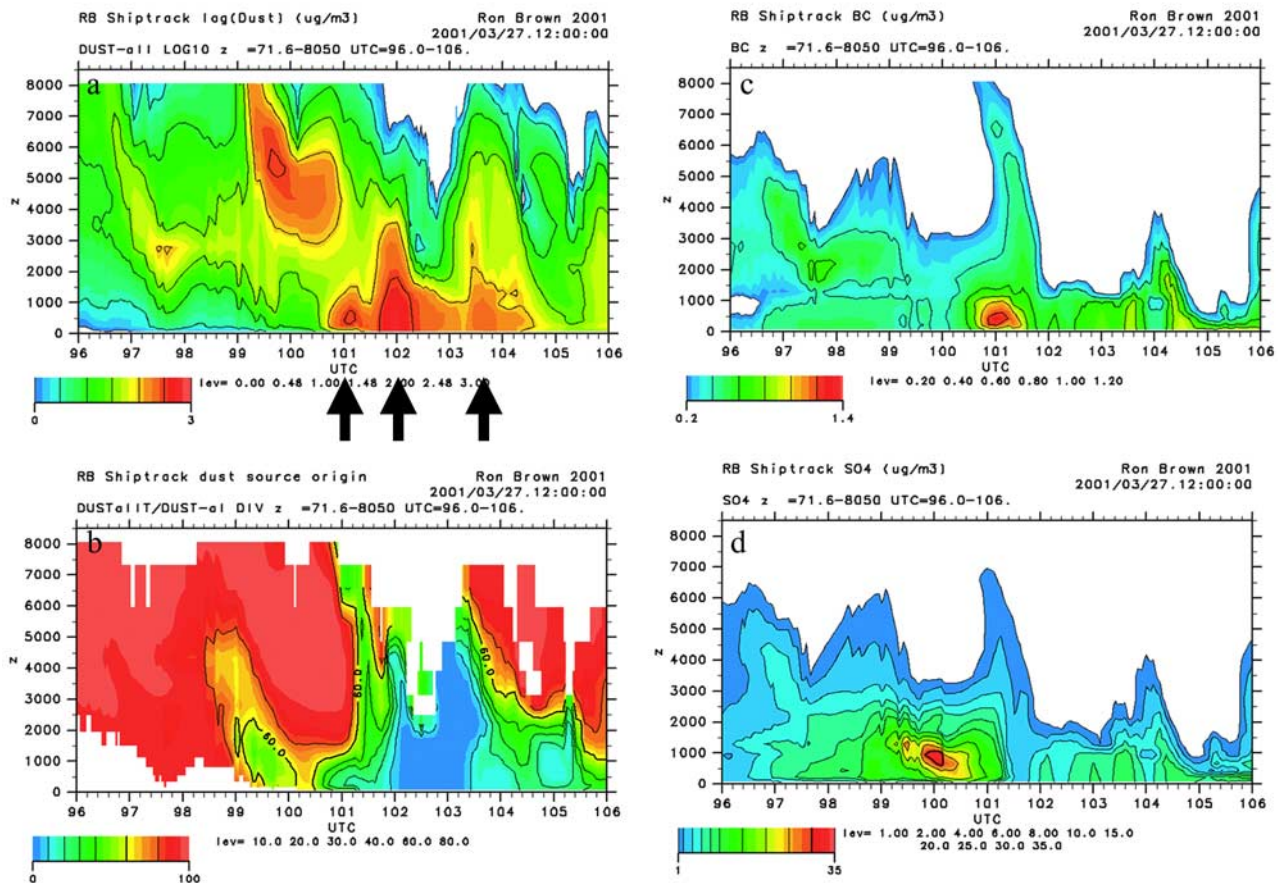


Figure 5. CFORS model output of (a) fine-mode dust concentration ($<2 \mu\text{m}$ diameter), (b) fraction of dust due to emissions from the Taklimakan desert, (c) total BC concentration, and (d) total nss sulfate concentration at the location of the ship between DOY 96 and 106. The arrows in Figure 5a point to the three pulses of dust observed at the ship. More detailed comparisons of the CFORS model output with the ship data are given by *Uno et al.* [2004].

The CFORS chemical transport model [*Uno et al.*, 2003] clearly captured (Figure 5a) the three pulses of dust that reached the surface along the ship’s track.

[47] Despite the high aerosol surface area during this “postfrontal” period, the aerosol number size distribution showed two events of newly formed particles (Figure 4) with total particle number concentrations ($D_p > 3\text{nm}$) of over $45,000 \text{ cm}^{-3}$. The high aerosol number concentrations were measured in the local midday hours on DOY 102 and 103 in air masses that had passed over the Korean Peninsula only a few hours earlier. Although this was clearly not Lagrangian sampling, the newly formed particles sampled at the ship appeared to “grow” in diameter at approximately 4 nm per hour over the following 2–3 hours. SO_2 concentrations in these air masses ranged from 0.5 to 5.0 ppb. Similar newly formed particle distributions were measured aboard the C-130 [*McNaughton et al.*, 2004]. *McNaughton et al.* [2004] concluded that these particles were formed at the top of the relatively stable “ocean boundary layer” and were then mixed down to the surface and up through the MBL by convective cells and turbulent eddies.

4.2. Chemical Properties

[48] Table 1 lists the mean concentrations, standard deviations, and absolute uncertainties of the major chemical species for the seven different air mass source regions. The submicron aerosol in the prefrontal air masses over the Sea of Japan (source regions 3 and 4) was dominated by ammonium sulfate with an average ammonium to non-sea-salt (nss) sulfate molar ratio of 1.7 ± 0.06 (mean and one standard deviation of the measurements during this time period). While the ammonium concentration was relatively constant during this period (Figure 6), the sulfate concentration increased by a factor of 4 when the back trajectories crossed the Miyakejima volcano lowering the ammonium sulfate ratio to 0.37 (Figure 7). Although the ship was 2–3 days downwind of the volcano, SO_2 concentrations were still 3 to 6 ppb (Figure 7). The volcanic plume with high sulfate concentrations was clearly evident in the CFORS regional aerosol model (Figure 5d) [*Uno et al.*, 2003]. The model, however, placed the Miyakajima plume above the shallow stable marine boundary layer. The predicted peak sulfate value in the plume ($\sim 30 \mu\text{g}/\text{m}^3$) was similar to that measured by the ship (Figure 6). While the model was able

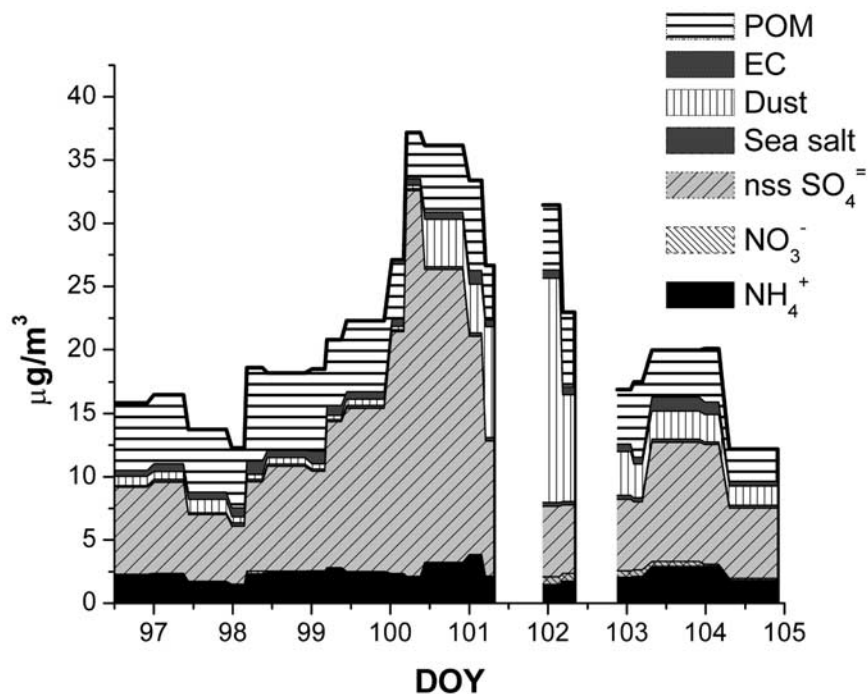


Figure 6. Submicron aerosol ($D_{aero} < 1.1 \mu\text{m}$ at 55% RH) chemical components measured in the MBL over the Sea of Japan. The missing data on DOY 101 and 102 were during periods when the ship was running downwind to reposition.

to qualitatively capture the volcano plume transport, it appears to have underestimated the downward mixing of this plume.

[49] The second most dominant component in the submicron prefrontal air mass was POM (Figure 6 and Table 1).

Mochida et al. [2003] have shown that approximately 20% of this POM was composed of oxygenated organic compounds (dicarboxylic acids and fatty acids). FTIR analysis of organic functional groups from each of the seven source regions showed that alkanes composed 23 to 69%, alkenes

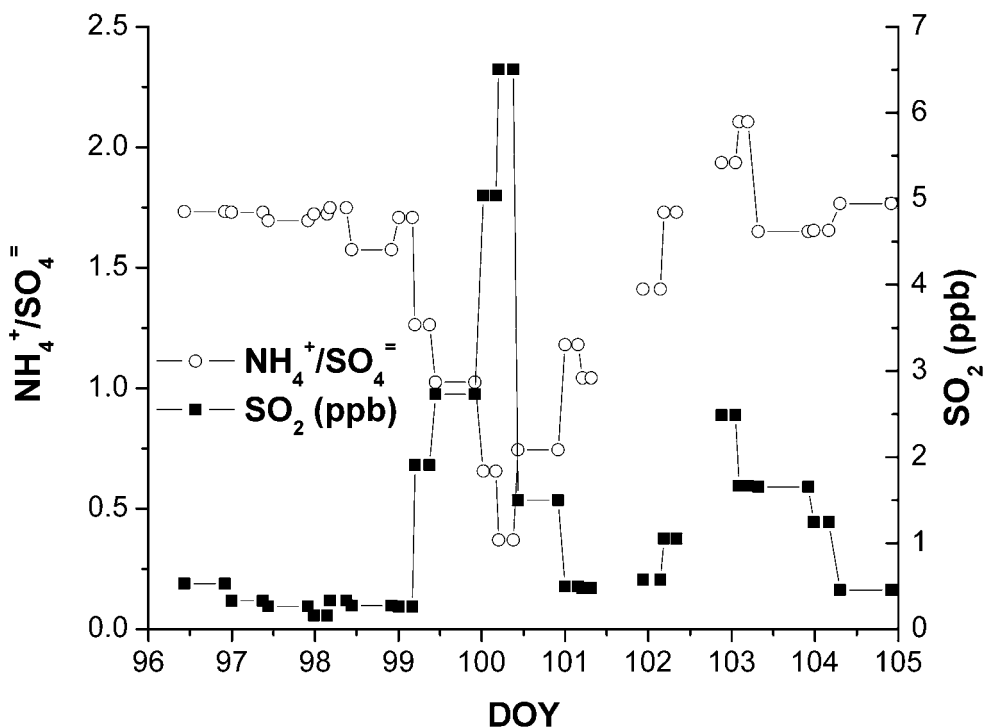


Figure 7. $\text{NH}_4^+/\text{nss SO}_4^-$ molar ratios and SO_2 concentrations averaged over the impactor periods (ppb). The sulfate aerosol was highly acidic in the high- SO_2 plume of the Miyakejima volcano.

Table 1. Concentrations, Standard Deviations, and Absolute Uncertainties of the Mean of Ionic Species, Inorganic Oxidized Material, and Carbonaceous Material in the Submicron and Supermicron Aerosol for the Different Air Mass Source Regions^a

Component	Source Region						
	1 (5–10 Samples)	2 (5–7 Samples)	3 (7 Samples)	4 (3 Samples)	5 (2 Samples)	6 (4 Samples)	7 (3 Samples)
NH ₄ ⁺	0.17 ± 0.16 (0.005)	1.3 ± 0.51 (0.029)	2.1 ± 0.40 (0.050)	2.4 ± 0.26 (0.073)	2.9 (0.13)	1.8 ± 0.29 (0.056)	2.6 ± 0.63 (0.091)
	0.010 ± 0.013 (0.001)	0.034 ± 0.057 (0.003)	0.078 ± 0.066 (0.005)	0.029 ± 0.037 (0.005)	0.051 (0.017)	0.58 ± 0.053 (0.020)	0.23 ± 0.13 (0.010)
NO ₃ ⁻	0.72 ± 0.58 (0.018)	5.0 ± 2.2 (0.12)	6.7 ± 1.3 (0.16)	18 ± 8.6 (0.60)	14 (0.61)	5.5 ± 0.13 (0.17)	8.1 ± 2.3 (0.29)
	0.31 ± 0.18 (0.019)	0.18 ± 0.085 (0.033)	0.19 ± 0.050 (0.040)	0.18 ± 0.040 (0.063)	0.27 (0.13)	0.31 ± 0.024 (0.076)	0.22 ± 0.008 (0.047)
nss SO ₄ ⁻	0.052 ± 0.065 (0.039)	0.16 ± 0.065 (0.079)	0.60 ± 0.24 (0.13)	0.34 ± 0.10 (0.17)	6.3 (1.6)	8.1 ± 7.1 (1.6)	1.6 ± 1.0 (0.34)
	0.39 ± 0.15 (0.053)	1.4 ± 0.56 (0.16)	5.4 ± 0.91 (0.45)	4.2 ± 0.72 (0.51)	5.6 (0.88)	5.5 ± 0.84 (0.67)	3.3 ± 0.92 (0.44)
Sea salt	0.070 ± 0.032 (0.031)	0.28 ± 0.042 (0.052)	0.71 ± 0.23 (0.090)	0.62 ± 0.12 (0.14)	0.81 (0.31)	0.60 ± 0.053 (0.18)	0.83 ± 0.41 (0.11)
	0.009 ± 0.007 (0.002)	0.039 ± 0.042 (0.003)	0.25 ± 0.11 (0.003)	0.044 ± 0.011 (0.005)	0.25 (0.011)	0.19 ± 0.047 (0.007)	0.26 ± 0.16 (0.004)
IOM (dust)	0.25 ± 0.21 (0.002)	1.6 ± 0.76 (0.004)	3.9 ± 1.5 (0.005)	1.3 ± 0.29 (0.008)	4.1 (0.017)	2.8 ± 0.70 (0.010)	6.5 ± 3.3 (0.006)
	0.001 ± 0.002 (0.000)	0.058 ± 0.060 (0.001)	0.17 ± 0.18 (0.001)	0.48 ± 0.23 (0.004)	2.4 (0.010)	0.26 ± 0.33 (0.003)	1.0 ± 1.3 (0.001)
POM	8.5 ± 4.7 (0.015)	5.0 ± 3.9 (0.029)	2.8 ± 1.5 (0.035)	1.5 ± 0.42 (0.056)	8.4 (0.11)	5.3 ± 3.4 (0.067)	7.9 ± 2.8 (0.035)
	1.3 ± 0.48 (0.22)	6.0 ± 2.0 (0.81)	9.1 ± 4.5 (1.2)	4.1 ± 0.62 (0.68)	86 (20)	66 ± 45 (12)	52 ± 31 (10)
EC	0.26 ± 0.096 (0.026)	1.3 ± 0.84 (0.083)	1.9 ± 0.35 (0.23)	1.2 ± 0.65 (0.31)	4.8 (0.88)	2.7 ± 1.8 (0.48)	2.0 ± 0.83 (0.31)
	0.014 ± 0.014 (0.021)	0.034 ± 0.11 (0.043)	0.25 ± 0.15 (0.088)	0.045 ± 0.10 (0.14)	0.65 (0.30)	0.16 ± 0.21 (0.18)	0.74 ± 0.41 (0.10)

^aConcentrations are given in $\mu\text{g m}^{-3}$. Standard deviations are $\pm 1\sigma$, and absolute uncertainties are at the 95% confidence level, shown in parentheses. IOM, inorganic oxidized material. Carbonaceous material shown is POM and EC. Submicron aerosol, $D_{\text{aero}} < 1.1 \mu\text{m}$ at 55% RH; supermicron aerosol, $1.1 < D_{\text{aero}} < 10 \mu\text{m}$ at 55% RH.

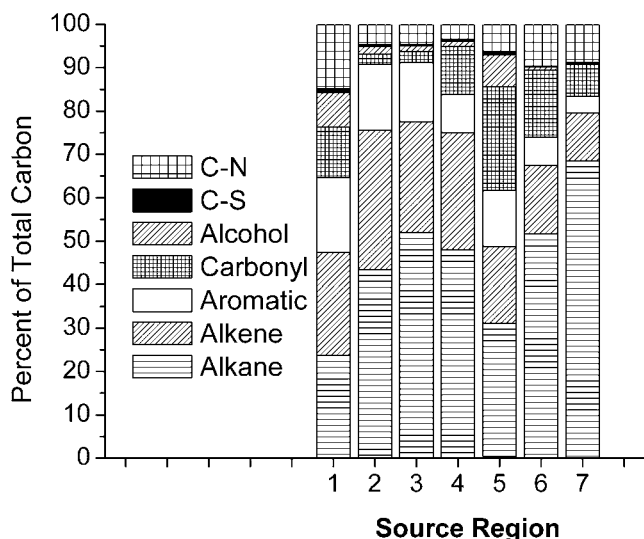


Figure 8. Percentage of each organic functional group to the total organic carbon for each source region based on the FTIR analysis.

composed 11 to 23%, aromatic compounds composed 4 to 17%, carbonyl compounds composed 2 to 24%, alcohols composed 0.2 to 8%, C-S bonded compounds composed 0.2 to 0.9%, and C-N bonded compounds composed 3 to 15% of the total organic carbon (Figure 8). The functional group data can be used to estimate an organic acid concentration by assuming an acid composition. Assuming the acid is 70% oxalic, 13% malonic, 10% succinic, and 7% a six-carbon acid (based on *Mochida et al.* [2003]), the acid

fraction of POM varied from 4.2% to 34% in the 7 source regions during ACE-Asia.

[50] The organic functional group data were also used to estimate the organic mass (POM) from the molecular mass of each functional group associated with the measured bond type [*Russell, 2003*]. The average POM/OC ratio in each region ranged from 1.3 to 1.6 with a calculated uncertainty of $\pm 10\%$ [*Russell, 2003*]. The overall cruise average POM/OC ratio was 1.4 ± 0.18 ($n = 40$). This is at the low end of the range of suggested by *Turpin and Lim* [2001] for urban environments and suggests a lower than normal percentage of oxygenated compounds.

[51] In addition to ammonium sulfate and POM, the submicron aerosol in the prefrontal air mass contained lesser amounts of elemental carbon, nitrate, sea salt and dust (Figure 6). Chemical transport models (Figure 5a; CFORS; *Uno et al.* [2003]), shipboard lidar [*Quinn et al., 2004*], and aircraft data [*Seinfeld et al., 2004*] showed a pronounced dust aerosol layer aloft during the period from DOY 99.3 and DOY 101. We hypothesize that the submicron and supermicron dust measured in the MBL during the prefrontal period (Figures 6 and 9) was a result of subsidence from this dust layer aloft. The CFORS model indicates a high percentage of Taklimakan desert dust in this layer (Figure 5a). Higher Mg/Al and Fe/Al ratios observed in the prefrontal air mass support the model results (Figure 10). In addition to dust, the coarse-mode aerosol contained sea salt, nitrate and POM. The sea salt in both the submicron and supermicron modes was highly depleted in chloride (Figure 11) from reaction with sulfuric and nitric acid vapors [*Clegg and Brimblecombe, 1985*].

[52] The passage of the frontal zone on DOY 100.8 brought elevated concentrations of submicron and super-

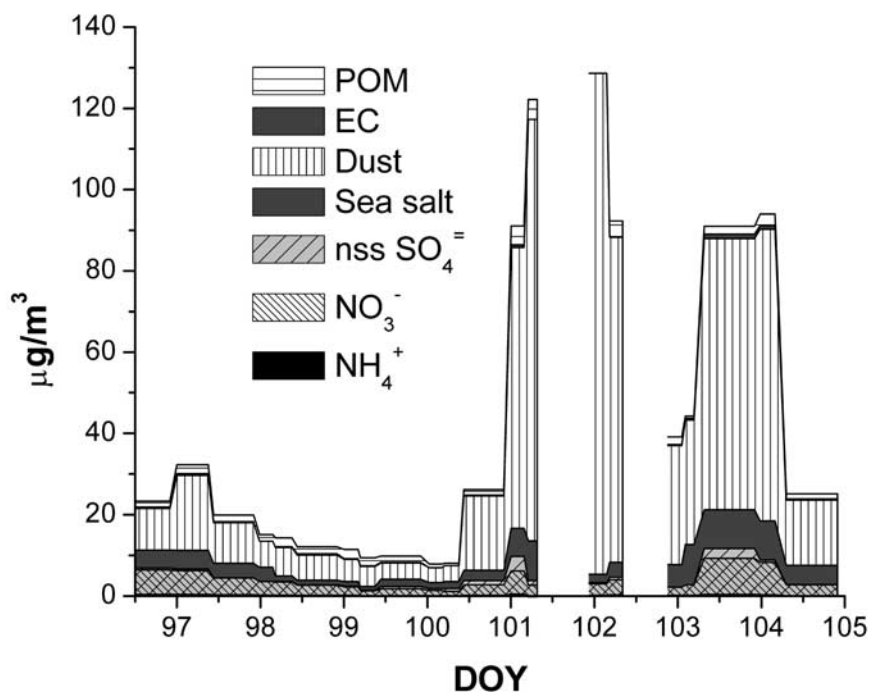


Figure 9. Supermicron aerosol ($1.1 \mu\text{m} < D_{\text{aero}} < 10 \mu\text{m}$ at 55% RH) chemical components measured in the MBL over the Sea of Japan. The missing data on DOY 101 and 102 were during periods when the ship was running downwind to reposition.

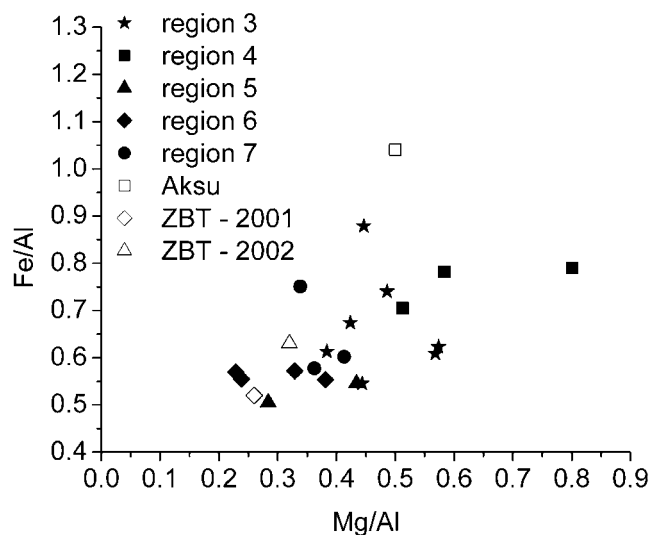


Figure 10. Elemental ratios (total aerosol) for source regions 3–7 as measured aboard *Ronald H. Brown* and reported in this paper (solid symbols), the Taklimakan desert (Aksu sampling station in Xinjiang [Zhang *et al.*, 2003b]), and Zhenbeitai (ZBT) at the southern edge of the Gobi desert (2001 data from Zhang *et al.* [2003b] and 2002 data from Alfaro *et al.* [2003]). The data measured near the sources are shown with open symbols. The higher Mg/Al and Fe/Al ratios observed in the prefrontal air masses (regions 3 and 4) are consistent with a higher percentage of dust from the Taklimakan desert.

micron (Figures 6 and 9) dust to the ship. The ATOFMS single particle data showed the highest dust particle number concentrations in the submicron size range (Figure 12). The particle volume, however, was either bimodal (source

region 5) or peaked in the supermicron size range (source region 6). Total (sub-10 μm) dust (IOM) concentrations measured on the ship reached $140 \mu\text{g}/\text{m}^3$ on DOY 102.0 which was approximately one third of the concentrations measured at Zhenbeitai (ZBT) near the city of Yulin ($380 \mu\text{g}/\text{m}^3$) by Zhang *et al.* [2003b] during this period. No significant difference in elemental composition could be detected between the various postfrontal dust episodes. Measured average Fe/Al (0.58 ± 0.07) and Mg/Al (0.33 ± 0.07) ratios in the postfrontal air masses were indicative of an aerosol source located in the “northern high desert” [Alfaro *et al.*, 2003] and are consistent with the CFORS model “Gobi desert” source (Figures 5a and 5b). The supermicron dust laden aerosol also contained sulfate and nitrate. The Cl^-/Na^+ ratio increased during this period suggesting that the sulfate and in particular the nitrate were less associated with the sea-salt aerosol and more associated with the higher-buffering-capacity dust aerosol [Tabazadeh *et al.*, 1998]. HNO_3 has been shown to undergo rapid uptake on metal oxides in dust [Underwood *et al.*, 2001]. The variable NO_3^-/Al mass ratios (0.25 to 1.65) during the postfrontal dust periods (source regions 5–7) suggest that most of the nitrate was a result of secondary aerosol formation. Single particle analysis during this period confirmed that the nitrate and dust were internally mixed (Figure 13). In the prefrontal air masses between 50 and 60% of the supermicron nitrate-containing particles were associated with sea salt. In the postfrontal air masses the percentages reversed and between 60 and 80% of the supermicron nitrate-containing particles were associated with dust (Figure 13). Supermicron sulfate behaved in a similar manner being associated with sea salt in the prefrontal air mass and with dust in the postfrontal air mass. This adds to the growing evidence that sorption and oxidation on dust particles is an important pathway for

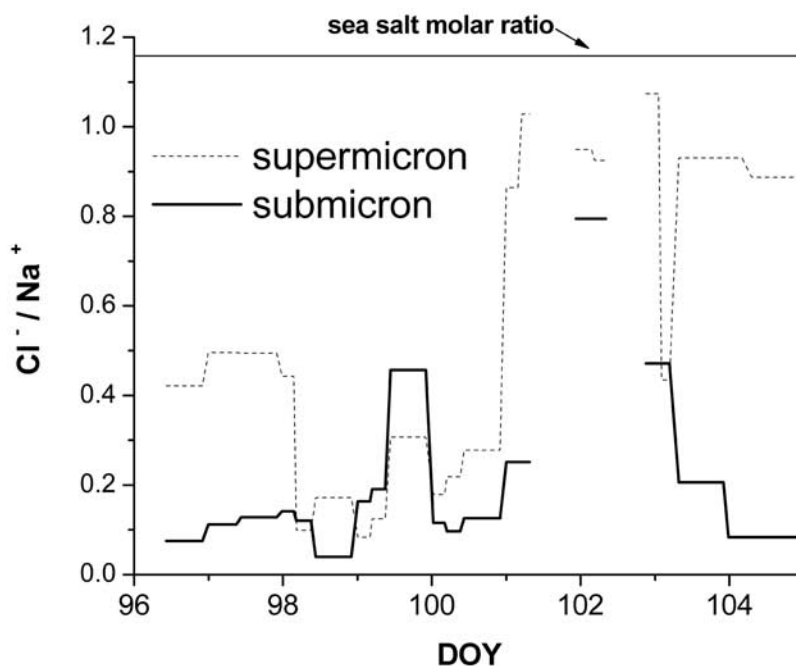


Figure 11. Submicron and supermicron Cl^-/Na^+ ratios showing the highly chloride depleted sea salt in the prefrontal air mass. The molar Cl^-/Na^+ ratio in unreacted sea salt is 1.18.

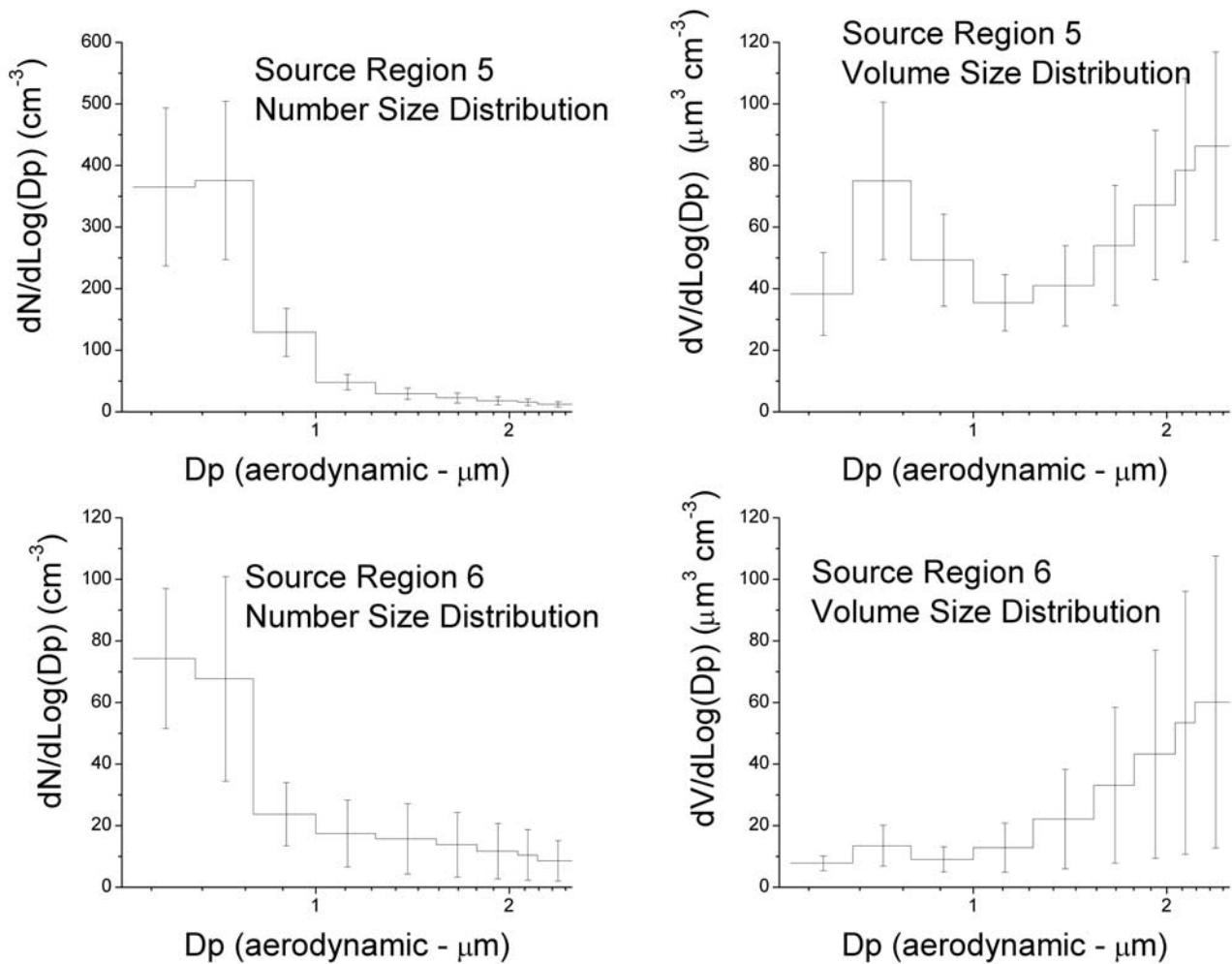


Figure 12. ATOFMS data showing the average and standard deviation of the number and volume distributions (aerodynamic diameters) of dust-containing particles during the source region 5 and 6 time periods (DOY 101 to 101.3 and DOY 101.8 to 103.4, respectively). The ATOFMS measures particles between 0.5 and 2.5 μm and hence samples only the smaller particles in the coarse-mode volume. The coarse-mode volume distribution during these periods peaked at approximately 4.0 μm aerodynamic diameter (2.5 μm geometric diameter, Figure 4).

sulfate and nitrate formation [Xiao *et al.*, 1997]. The dust sampled on the ship during this period, however, had not absorbed all the available SO_2 as concentrations in the postfrontal air masses still contained 0.5–2.5 ppb of SO_2 (Figure 7).

[53] The initial frontal/dust sample (DOY 101.00–101.15) and the source region 7 samples (Shanghai, DOY 103.3 and 104.2) also contained elevated concentrations of elemental carbon (Table 1). Similar to the results at Gosan, Korea [Chuang *et al.*, 2003], a significant fraction of the elemental carbon (up to 48% on DOY 103) existed in the supermicron mode during this period. Total nss noncrustal potassium was also elevated in these samples (0.97 and 0.99 $\mu\text{g}/\text{m}^3$ in regions 5 and 7 respectively vs. a mean concentration of $0.30 \pm 0.12 \mu\text{g}/\text{m}^3$ in regions 3, 4, and 6) suggesting a biomass/biofuel source [Guazzotti *et al.*, 2003]. The CFORS regional model underestimated elemental carbon concentrations along the ship's track by 50% (Figure 5c), but quantitatively captured the elevated potassium concentrations (not shown). Elemental carbon and

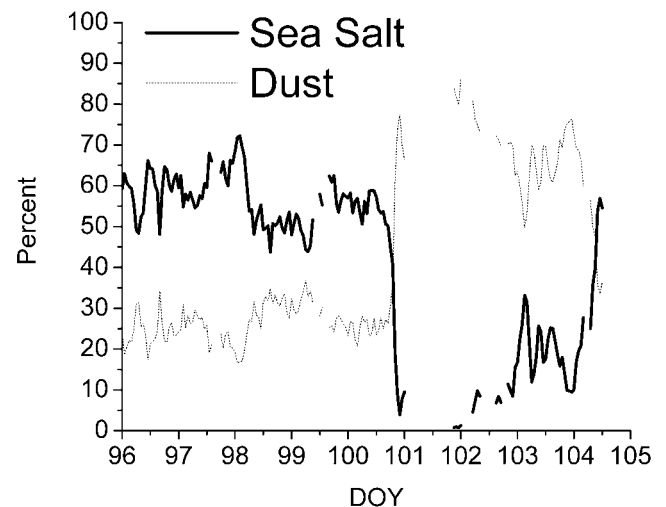


Figure 13. ATOFMS data showing the percent of supermicrometer nitrate particles associated with dust or sea salt.

potassium are correlated in the model, supporting the hypothesis that the outflow from source region 7 is rich in biofuel emissions. While biofuel emissions represent more than 50% of the elemental carbon source in this region, they are also highly uncertain, and may be underestimated by as much as a factor of 2 in the present inventory [Carmichael *et al.*, 2003].

5. Summary

[54] The prefrontal and postfrontal air masses sampled aboard *Ronald H. Brown* between 6 and 15 April 2001 illustrate the different chemical sources/mixtures off the coast of Asia resulting from the contrasting meteorological transport patterns. The aerosol number and volume size distributions in the prefrontal MBL polluted air mass were dominated by aerosols in the accumulation-mode size range composed of ammonium sulfate (average molar ratio of 1.7 ± 0.06) and organic and elemental carbon. The coarse-mode, MBL supermicron aerosol during this period contained sea salt, nitrate, organic carbon and subsiding dust. The sea salt in both the submicron and supermicron aerosol was highly reacted with the pollution aerosol depleting $77 \pm 12\%$ of the total chloride. On 9 and 10 April (DOY 99 and 100) the low-level back trajectories from the ship crossed the Miyakejima volcano. Although the ship was 2–3 days downwind of the volcano in the Sea of Japan, 30 min mean SO_2 concentrations measured at the ship reached 11.7 ppb and the measured aerosol was much more acidic (ammonium sulfate molar ratios dropped to 0.37).

[55] The aerosol volume size distributions in the post-frontal MBL air masses were dominated by the coarse-mode-containing dust and lesser amounts of nitrate, sea salt, sulfate, and organic and elemental carbon. The submicron aerosol also contained appreciable concentrations of dust as well as sulfate, ammonium, organic and elemental carbon, and nitrate. At times the dust-laden air mass contained elevated concentrations of elemental carbon and nss noncrustal potassium, markers of biomass or biofuel burning. The submicron and supermicron sea-salt aerosol was much less depleted in chloride ($27 \pm 15\%$) during this high-dust period. The higher Cl^-/Na^+ ratios and the single particle analysis suggest that the sulfuric and nitric acid were preferentially associated with the high concentrations of dust because of its high buffering capacity.

[56] The most distinguishing characteristic of the Asian aerosol is the high concentration of dust and it is the dust that controls the aerosol optical properties [Quinn *et al.*, 2004]. However, the results presented here illustrate the many other aerosol sources in the region (volcanic, biomass/biofuel burning, industrial) and the interaction of these pollutant species with both dust and sea salt. The supermicron dust and sea salt with higher settling velocities and thus shorter atmospheric residence times provide a major sink for pollution species (nitric and sulfuric acid, organic and elemental carbon).

[57] The MBL aerosol properties and controlling processes described here provide data to evaluate and refine chemical transport models. Accurately modeling these meteorological regimes, the strong point source and regional emissions, and

the atmospheric transport and transformation processes are critical for calculating the regional aerosol radiative and cloud nucleating properties.

[58] **Acknowledgments.** We thank the officers and crew of NOAA R/V *Ronald H. Brown* for their cooperation and enthusiasm, the UCAR Joint Office for Scientific Support for their meteorological and operational support, and Drew Hamilton for logistical support. This research was funded by the Aerosol Project of the NOAA Climate and Global Change Program, the NOAA Office of Oceanic and Atmospheric Research, the NSF Atmospheric Chemistry Program, and the NASA Global Aerosol Climatology Project. This research is a contribution to the International Global Atmospheric Chemistry (IGAC) Core Project of the International Geosphere Biosphere Program (IGBP) and is part of the IGAC Aerosol Characterization Experiments (ACE). This is NOAA/PMEL contribution 2596 and JISAO contribution 1013.

References

- Alfaro, S. C., et al. (2003), Chemical and optical characterization of aerosols measured in spring 2002 at the ACE-Asia supersite, Zhenbeitai, China, *J. Geophys. Res.*, *108*(D23), 8641, doi:10.1029/2002JD003214.
- Anderson, T. L., S. J. Masonis, D. S. Covert, N. C. Ahlquist, S. G. Howell, A. D. Clarke, and C. S. McNaughton (2003), Variability of aerosol optical properties derived from in situ aircraft measurements during ACE-Asia, *J. Geophys. Res.*, *108*(D23), 8647, doi:10.1029/2002JD003247.
- Angelino, S., D. T. Suess, and K. A. Prather (2001), Formation of aerosol particles from reactions of secondary and tertiary alkylamines: Characterization by aerosol time-of-flight mass spectrometry, *Environ. Sci. Technol.*, *35*, 3130–3138.
- Arndt, R. L., G. R. Carmichael, D. G. Streets, and N. Bhatti (1997), Sulfur dioxide emissions and sectorial contributions to sulfur deposition in Asia, *Atmos. Environ.*, *31*, 1553–1572.
- Bates, T. S., D. J. Coffman, D. S. Covert, and P. K. Quinn (2002), Regional marine boundary layer aerosol size distributions in the Indian, Atlantic, and Pacific Oceans: A comparison of INDOEX measurements with ACE-1, ACE-2, and Aerosols99, *J. Geophys. Res.*, *107*(D19), 8026, doi:10.1029/2001JD001174.
- Berner, A., C. Lurzer, F. Pohl, O. Preining, and P. Wagner (1979), The size distribution of the urban aerosol in Vienna, *Sci. Total Environ.*, *13*, 245–261.
- Bey, I., D. J. Jacob, J. A. Logan, and R. M. Yantosca (2001), Asian chemical outflow to the Pacific in spring: Origins, pathways, and budgets, *J. Geophys. Res.*, *106*, 23,097–23,113.
- Birch, M. E., and R. A. Cary (1996), Elemental carbon-based method for monitoring occupational exposures to particulate diesel exhaust, *Aerosol Sci. Technol.*, *25*, 221–241.
- Braaten, D. A., and T. A. Cahill (1986), Size and composition of Asian dust transported to Hawaii, *Atmos. Environ.*, *20*, 1105–1109.
- Carmichael, G. R., et al. (2003), Evaluating regional emission estimates using the TRACE-P observations, *J. Geophys. Res.*, *108*(D21), 8810, doi:10.1029/2002JD003116.
- Carrico, C. M., P. Kus, M. J. Rood, P. K. Quinn, and T. S. Bates (2003), Mixtures of pollution, dust, sea salt, and volcanic aerosol during ACE-Asia: Radiative properties as a function of relative humidity, *J. Geophys. Res.*, *108*(D23), 8650, doi:10.1029/2003JD003405.
- Cheng, Y. S., B. T. Chen, and H. C. Yeh (1990), Behavior of isometric nonspherical aerosol-particles in the aerodynamic particle sizer, *J. Aerosol Sci.*, *21*, 701–710.
- Cheng, Y. S., B. T. Chen, H. C. Yeh, I. A. Marshall, J. P. Mitchell, and W. D. Griffiths (1993), Behavior of compact nonspherical particles in the TSI aerodynamic particle sizer model APS33B: Ultra-Stokesian drag forces, *Aerosol Sci. Technol.*, *19*, 255–267.
- Chin, M., P. Ginoux, R. Lucchesi, B. Huebert, R. Weber, T. Anderson, S. Masonis, B. Blomquist, A. Bandy, and D. Thornton (2003), A global aerosol model forecast for the ACE-Asia field experiment, *J. Geophys. Res.*, *108*(D23), 8654, doi:10.1029/2003JD003642.
- Chuang, P. Y., R. M. Duvall, M. S. Bae, A. Jefferson, J. J. Schauer, H. Yang, J. Z. Yu, and J. Kim (2003), Observations of elemental carbon and absorption during ACE-Asia and implications for aerosol radiative properties and climate forcing, *J. Geophys. Res.*, *108*(D23), 8634, doi:10.1029/2002JD003254.
- Clegg, S. L., and P. Brimblecombe (1985), Potential degassing of hydrogen chloride from acidified sodium chloride droplets, *Atmos. Environ.*, *19*, 465–470.
- Conant, W. C., J. H. Seinfeld, J. Wang, G. R. Carmichael, Y. Tang, I. Uno, P. J. Flatau, K. M. Markowicz, and P. K. Quinn (2003), A model for the

- radiative forcing during ACE-Asia derived from CIRPAS Twin Otter and R/V *Ronald H. Brown* data and comparison with observations, *J. Geophys. Res.*, *108*(D23), 8661, doi:10.1029/2002JD003260.
- Covert, D. S., A. Wiedensohler, and L. M. Russell (1997), Particle charging and transmission efficiencies of aerosol charge neutralizers, *Aerosol Sci. Technol.*, *27*, 208–214.
- Draxler, R. R. (1992), Hybrid Single-Particle Lagrangian Integrated Trajectories (HY-SPLIT): Version 3.0, User's guide and model description, *Tech. Rep. ERL ARL-195*, Natl. Oceanic and Atmos. Admin., Silver Spring, Md.
- Feely, R. A., G. J. Massoth, and G. T. Lebon (1991), Sampling of marine particulate matter and analysis by X-ray fluorescence spectrometry, in *Marine Particles: Analysis and Characterization*, *Geophys. Monogr. Ser.*, vol. 63, edited by D. C. Hurd and D. W. Spencer, pp. 251–257, AGU, Washington, D. C.
- Feely, R. A., E. T. Baker, G. T. Lebon, J. F. Gendron, G. J. Massoth, and C. W. Mordy (1998), Chemical variations of hydrothermal particles in the 1996 Gorda Ridge Event and chronic plumes, *Deep Sea Res., Part II*, *45*, 2637–2664.
- Gard, E., et al. (1997), Real-time analysis of individual atmospheric aerosol particles: Design and performance of a portable ATOFMS, *Anal. Chem.*, *69*, 4083–4091.
- Gard, E. E., et al. (1998), Direct observation of heterogeneous chemistry in the atmosphere, *Science*, *279*, 1184–1187.
- Guazzotti, S. A., K. R. Coffee, and K. A. Prather (2001), Continuous measurements of size-resolved particle chemistry during INDOEX-Intensive Field Phase 99, *J. Geophys. Res.*, *106*, 28,607–28,627.
- Guazzotti, S. A., et al. (2003), Characterization of carbonaceous aerosols outflow from India and Arabia: Biomass/biofuel burning and fossil fuel combustion, *J. Geophys. Res.*, *108*(D15), 4485, doi:10.1029/2002JD003277.
- Holland, H. D. (1978), *The Chemistry of the Atmosphere and Oceans*, p. 154, John Wiley, Hoboken, N. J.
- Hoppel, W. A., G. M. Frick, and R. E. Larson (1986), Effect of nonprecipitating clouds on the aerosol size distribution in the marine boundary layer, *Geophys. Res. Lett.*, *13*, 125–128.
- Huebert, B. J., T. Bates, P. B. Russell, G. Shi, Y. J. Kim, K. Kawamura, G. Carmichael, and T. Nakajima (2003), An overview of ACE-Asia: Strategies for quantifying the relationships between Asian aerosols and their climatic impacts, *J. Geophys. Res.*, *108*(D23), 8633, doi:10.1029/2003JD003550.
- Jahn, B.-M., S. Gallet, and J. Han (2001), Geochemistry of the Xining, Xifeng and Jixian section, Loess Plateau of China: Eolian dust provenance and paleosol evolution during the last 140 ka, *Chem. Geol.*, *178*, 71–94.
- Liu, D. Y., K. A. Prather, and S. V. Hering (2000), Variations in the size and chemical composition of nitrate-containing particles in Riverside, CA, *Aerosol Sci. Technol.*, *33*, 71–86.
- Mader, B. T., et al. (2003), Sampling methods used for the collection of particle-phase organic and elemental carbon during ACE-Asia, *Atmos. Environ.*, *37*, 1435–1449.
- Malm, W. C., J. F. Sisler, D. Huffman, R. A. Eldred, and T. A. Cahill (1994), Spatial and seasonal trends in particle concentration and optical extinction in the United States, *J. Geophys. Res.*, *99*, 1347–1370.
- Maria, S. F., L. M. Russell, B. J. Turpin, and R. J. Porcja (2002), FTIR measurements of functional groups and organic mass in aerosol samples over the Caribbean, *Atmos. Environ.*, *36*, 5185–5196.
- McNaughton, C. S., et al. (2004), Spatial distribution and size evolution of particles in Asian outflow: Significance of primary and secondary aerosols during ACE-Asia and TRACE-P, *J. Geophys. Res.*, doi:10.1029/2003JD003528, in press.
- Mochida, M., K. Kawamura, N. Umemoto, M. Kobayashi, S. Matsunaga, H.-J. Lim, B. J. Turpin, T. S. Bates, and B. R. T. Simoneit (2003), Spatial distributions of oxygenated organic compounds (dicarboxylic acids, fatty acids and levoglucosan) in marine aerosols over the western Pacific and off the coast of east Asia: Continental outflow of organic aerosols during the ACE-Asia campaign, *J. Geophys. Res.*, *108*(D23), 8638, doi:10.1029/2002JD003249.
- Noble, C. A., and K. A. Prather (1996), Real-time measurement of correlated size and composition profiles of individual atmospheric aerosol particles, *Environ. Sci. Technol.*, *30*, 2667–2680.
- Perry, K. D., T. A. Cahill, R. A. Eldred, D. D. Dutcher, and T. E. Gill (1997), Long-range transport of North African dust to the eastern United States, *J. Geophys. Res.*, *102*, 1225–1238.
- Prather, K. A., et al. (1994), Real-time characterization of individual aerosol particles using time of flight mass spectrometry, *Anal. Chem.*, *66*, 1403–1407.
- Quinn, P. K., and D. J. Coffman (1998), Local closure during ACE 1: Aerosol mass concentration and scattering and backscattering coefficients, *J. Geophys. Res.*, *103*, 16,575–16,596.
- Quinn, P. K., D. J. Coffman, V. N. Kapustin, T. S. Bates, and D. S. Covert (1998b), Aerosol optical properties in the marine boundary layer during ACE 1 and the underlying chemical and physical aerosol properties, *J. Geophys. Res.*, *103*, 16,547–16,563.
- Quinn, P. K., et al. (2004), Aerosol optical properties measured on board the *Ronald H. Brown* during ACE-Asia as a function of aerosol chemical composition and source region, *J. Geophys. Res.*, doi:10.1029/2003JD004010, in press.
- Russell, L. M. (2003), Aerosol organic-mass-to-organic-carbon ratio measurements, *Environ. Sci. Technol.*, *37*, 2982–2987.
- Savoie, D. L., and J. M. Prospero (1980), Water-soluble potassium, calcium, and magnesium in the aerosols over the tropical North Atlantic, *J. Geophys. Res.*, *85*, 385–392.
- Schauer, J. J., et al. (2003), ACE Asia intercomparison of a thermal-optical method for the determination of particle-phase organic and elemental carbon, *Environ. Sci. Technol.*, *37*, 993–1001, doi:10.1021/es020622f.
- Seinfeld, J. H. (1986), *Atmospheric Chemistry and Physics of Air Pollution*, 296 pp., John Wiley, Hoboken, N. J.
- Seinfeld, J. H., et al. (2004), Regional climatic and atmospheric chemical effects of Asian dust and pollution, *Bull. Am. Meteorol. Soc.*, *85*, 367–380, doi:10.1175/BAMS-85-3-367.
- Silva, P. J., D. Y. Liu, C. A. Noble, and K. A. Prather (1999), Size and chemical characterization of individual particles resulting from biomass burning of local Southern California species, *Environ. Sci. Technol.*, *33*, 3068–3076.
- Sioutas, C., P. Koutrakis, and R. M. Burton (1994), Development of a low cutpoint slit virtual impactor for sampling ambient fine particles, *J. Aerosol Sci.*, *25*, 1321–1330.
- Stratman, F., and A. Wiedensohler (1997), A new data inversion algorithm for DMPS measurements, *J. Aerosol Sci.*, *27*, 339–340.
- Streets, D. G., S. K. Guttikunda, and G. R. Carmichael (2000), The growing contribution of sulfur emissions from ships in Asian waters, 1988–1995, *Atmos. Environ.*, *34*, 4425–4439.
- Streets, D. G., S. Gupta, S. T. Waldhoff, M. Q. Wang, T. C. Bond, and B. Yiyun (2001), Black carbon emissions in China, *Atmos. Environ.*, *35*, 4281–4296.
- Sun, J., M. Zhang, and T. Liu (2001), Spatial and temporal characteristics of dust storms in China and its surrounding regions, 1960–1999: Relations to source area and climate, *J. Geophys. Res.*, *106*, 10,325–10,333.
- Tabazadeh, A., M. Z. Jacobson, H. B. Singh, O. B. Toon, J. S. Lin, R. B. Chazfield, A. N. Thakur, T. W. Talbot, and J. E. Dibb (1998), Nitric acid scavenging by mineral and biomass burning aerosols, *Geophys. Res. Lett.*, *25*, 4185–4188.
- Turpin, B. J., and H. Lim (2001), Species contribution to PM_{2.5} concentrations: Revisiting common assumptions for estimating organic mass, *Aerosol Sci. Technol.*, *35*, 602–610.
- Turpin, B. J., J. J. Huntzicker, and S. V. Hering (1994), Investigation of organic aerosol sampling artifacts in the Los Angeles Basin, *Atmos. Environ.*, *28*, 23,061–23,071.
- Turpin, B. J., P. Saxena, and E. Andrews (2000), Measuring and simulating particulate organics in the atmosphere: Problems and prospects, *Atmos. Environ.*, *34*, 2983–3013.
- Underwood, G. M., C. H. Song, M. Phadnis, G. R. Carmichael, and V. H. Grassian (2001), Heterogeneous reactions of NO₂ and HNO₃ on oxides and mineral dust: A combined laboratory and modeling study, *J. Geophys. Res.*, *106*, 18,055–18,066.
- Uno, I., et al. (2003), Regional chemical weather forecasting system CFORS: Model descriptions and analysis of surface observations at Japanese island stations during the ACE-Asia experiment, *J. Geophys. Res.*, *108*(D23), 8668, doi:10.1029/2002JD002845.
- Uno, I., et al. (2004), Numerical study of Asian dust transport during the springtime of 2001 simulated with the CFORS model, *J. Geophys. Res.*, doi:10.1029/2003JD004222, in press.
- Wang, H. C., and W. John (1987), Particle density correction for the aerodynamic particle sizer, *Aerosol Sci. Technol.*, *6*, 191–198.
- Wang, J., et al. (2002), Clear-column radiative closure during ACE-Asia: Comparison of multiwavelength extinction derived from particle size and composition with results from Sun photometry, *J. Geophys. Res.*, *107*(D23), 4688, doi:10.1029/2002JD002465.
- Wiedensohler, A., et al. (1997), Intercomparison study of the size-dependent counting efficiency of 26 condensation particle counters, *Aerosol Sci. Technol.*, *27*, 224–254.
- Winklmayr, W., G. P. Reischl, A. O. Lindner, and A. Berner (1991), A new electromobility spectrometer for the measurement of aerosol size distributions in the size range from 1 to 1000 nm, *J. Aerosol Sci.*, *22*, 289–296.
- Xiao, H., G. R. Carmichael, J. Dürchenwald, D. Thornton, and A. Bandy (1997), Long-range transport of SO_x and dust in east Asia during the PEM B experiment, *J. Geophys. Res.*, *102*, 28,589–28,612.

- Xuan, J., and I. N. Sokolik (2002), Characterization of sources and emission rates of mineral dust in northern China, *Atmos. Environ.*, *36*, 4863–4876.
- Zhang, X. Y., S. L. Gong, R. Arimoto, Z. X. Shen, F. M. Mei, D. Wang, and Y. Cheng (2003a), Characterization and temporal variation of Asian dust aerosol from a site in the northern Chinese deserts, *J. Atmos. Chem.*, *44*, 241–257.
- Zhang, X. Y., S. L. Gong, Z. X. Shen, F. M. Mei, X. X. Xi, L. C. Liu, Z. J. Zhou, D. Wang, Y. Q. Wang, and Y. Cheng (2003b), Characterization of soil dust aerosol in China and its transport and distribution during 2001 ACE-Asia, *J. Geophys. Res.*, *108*(D9), 4261, doi:10.1029/2002JD002632.
-
- T. S. Bates and P. K. Quinn, Pacific Marine Environmental Laboratory (PMEL), NOAA, 7600 Sand Point Way NE, Seattle, WA 98115, USA. (tim.bates@noaa.gov; patricia.k.quinn@noaa.gov)
- G. R. Carmichael, Center for Global and Regional Environmental Research, University of Iowa, Iowa City, IA 52242, USA. (gcarmich@icaen.uiowa.edu)
- D. J. Coffman, J. E. Johnson, and T. L. Miller, Joint Institute for the Study of the Atmosphere and Ocean (JISAO), University of Washington, Box 354235, Seattle, WA 98195-4235, USA. (djcoffma@u.washington.edu; jjalki@u.washington.edu; tlm4@u.washington.edu)
- D. S. Covert, Department of Atmospheric Sciences, University of Washington, 408 ATG Building, Box 351640, Seattle, WA 98195-1640, USA. (dcovert@u.washington.edu)
- S. A. Guazzotti, K. A. Prather, and D. A. Sodeman, Department of Chemistry and Biochemistry, University of California, San Diego, 2040 Urey Hall Addition, 9500 Gilman Drive, MC 0332, La Jolla, CA 92093, USA. (serad@chem.ucsd.edu; kprather@ucsd.edu; dsodeman@chem.ucsd.edu)
- J. T. Merrill, Center for Atmospheric Chemistry Studies, Graduate School of Oceanography, University of Rhode Island, South Ferry Road, Narragansett, RI 02882, USA. (jmerrill@boreas.gso.uri.edu)
- M. Rivera, Department of Environmental Engineering, Princeton University, Princeton, NJ 08548, USA.
- L. M. Russell, Department of Chemical Engineering, Princeton University, A317 Engineering Quadrangle, Princeton, NJ 08548, USA. (lrussell@princeton.edu)
- I. Uno, Research Institute for Applied Mechanics, Kyushu University, Kasuga Park 6-1, Kasuga 816-8580, Japan. (iuno@riam.kyushu-u.ac.jp)